MSc

2.º CICLO

FCUP
2015

U.PORTO

Nanofabrication of Pd nanowires and dendrites for H_2(g) sensing

Pedro Miguel da Rocha Rodrigues

FC

U.PORTO

FACULDADE DE CIÊNCIAS
UNIVERSIDADE DO PORTO

Nanofabrication of Pd nanowires and dendrites for H_2(g) sensing

Pedro Miguel da Rocha Rodrigues

Dissertação de Mestrado apresentada à
Faculdade de Ciências da Universidade do Porto em Física

2015

U.PORTO

FACULDADE DE CIÊNCIAS
UNIVERSIDADE DO PORTO

MSc

Nanofabrication of Pd nanowires and dendrites for H_2(g) sensing

Pedro Miguel da Rocha Rodrigues
M.Sc. in Physics
Department of Physics and Astronomy
2015

Supervisor
José Miguel Mesquita Teixeira, Post-Doctoral Researcher at IFIMUP-IN,
Department of Physics and Astronomy, Faculty of Science, University of Oporto

U.PORTO

FACULDADE DE CIÊNCIAS
UNIVERSIDADE DO PORTO

Todas as correções determinadas pelo júri, e só essas, foram efetuadas.

O Presidente do Júri,

Porto, _____/_____/_____

Nanofabrication of Pd nanowires and dendrites for H_2(g) sensing

Pedro Miguel Rocha Rodrigues

Thesis submitted to the
Faculty of Sciences of the University of Porto
in partial fulfillment of the requirements
for the degree of
Master in Physics

Supervisor: José Miguel Mesquita Teixeira,

Department of Physics and Astronomy
Faculty of Sciences of the University of Porto
September 2015

Acknowledgements

Prestes a terminar esta etapa resta-me agradecer a todos que de alguma forma contribuíram e a tornaram possível.

Ao meu orientador José Miguel Teixeira, por toda a dedicação e disponibilidade, por ter confiado em mim desde o primeiro momento e me ter dado a oportunidade de integrar numa equipa de investigação. Pelo empenho inspirador, como pessoa e como cientista. Pelos incansáveis incentivos nos momentos de maior dificuldade, por todas as sugestões e discussões e por continuar sempre a puxar por mim um grandíssimo e sincero obrigado.

Ao Aurélio Hierro-Rodriguez, sem quem este trabalho não teria a metade do gozo! O entusiasmo contagiante com que fala de qualquer assunto de física, pelas histórias, pela partilha na aventura do desconhecido, pelo companheirismo e por toda ajuda um enorme obrigado.

Á Célia Sousa pela primeira primeira e segunda anodização, pelo trabalho pioneiro no estudo das dendrites sem o qual este trabalho não seria possível, mas acima de tudo por toda a simpatia e disponibilidade.

Ao João Azevedo por toda a ajuda e apoio, desde a primeira eletrodeposição e a toda a restante ajuda desde então.

Aos restantes membros do laboratório da Alumina, à Arlete, à Paula, ao Vanji, à Mariana, ao Gonçalo pela disponibilidade, por todo o apoio e por me receberem de braços abertos no laboratório.

Aos restantes membros da colaboração entre o INESC-CAP e o IFIMUP-IN da qual parte deste trabalho se baseou, ao Aurélio Hierro-Rodriguez, ao Ivo Leite, ao Pedro Fernandes, ao professor José Luís dos Santos, ao professor João Pedro Araújo, ao meu orientador José Teixeira e ao professor Ariel Guerreiro pela enorme contribuição na compreensão da interação da luz com na Alumina Nanoporosa e o Paládio durante a sua hidrogenação.

Ao CEMUP e ao mestre Rui Rocha pela paciência e profissionalismo na obtenção das imagens de SEM que estão presentes nesta tese.

Ao professor João Pedro Araújo por todo o apoio e dedicação.

Ao departamento de Física e Astronomia da Universidade do Porto, ao IFIMUP-IN e ao INESC-CAP que pelo seu historial de excelência, me proporcionaram as condições de acolhimento para que este trabalho se realiza-se.

Aos meus companheiros ao Tiago, à Tenessa, ao Daniel e ao Sílvio.

E finalmente aos meus pais, por todo o seu esforço e apoio, ao meu irmão pela animação nos melhores e piores momentos. A vós vos dedico o que de melhor houver nesta tese.

Resumo

Com o recente desenvolvimento das células de combustível o Hidrogénio tornou-se um dos promissores candidatos a assumir o papel dos combustíveis fosseis para os veículos do futuro. Contudo a sua implementação acarreta riscos de segurança, quando presente na atmosfera a concentrações superiores a 4% (v/v) cria uma mistura altamente infamável e explosiva. De tal forma se estimulou a investigação e o desenvolvimento de uma nova geração de sensores, mais baratos e capazes de monitorizar concentrações de H_2(g) de uma forma mais rápida e segura, de forma a detetar eventuais fugas e prevenir explosões. Neste intuito, a capacidade do catalítica do Paládio, em dissociar a molécula de H_2 na sua superfície e incorporar os átomos de H na sua estrutura cristalina torna-o um dos materiais ideais no desenvolvimento de sensores de estado sólido de H_2(g). O auxílio da Nanotecnologia nomeadamente na fabricação de nanopartículas, nanotubos, nanofios de Pd para sensorização de H_2(g) torna-se vantajoso, não só por permitir um aumento do rácio superfície/volume mas também por permitir explorar possíveis efeitos de confinamento.

Na primeira parte deste trabalho apresenta-se a fabricação de nanofios e dendrites de Paládio com recurso à electrodeposição pulsada em *templates* de alumina nanoporosa. Um método *self-assembly* com a vantagem de ser facilmente implementado a nível industrial. Apresentam-se alguns dos resultados obtidos e considerações sobre o uso desta técnica para a deposição específica de Paládio. É também discutido a monotorização, em tempo real, da qualidade do crescimento e o comprimento dos nanofios através da cor das amostras, originada por fenómenos de interferência de Fabry-Pérot.

Na segunda parte apresenta-se a funcionalização das amostras preparadas para a sensorização de H_2(g). Foi efetuada a caracterização da resposta ótica em transmissão das nanoestruturas de Pd face a uma exposição de H_2(g) para uma gama de concentrações de 1 a 12% no ar (v/v). É tida em consideração a transição de fase α-β do Pd hidrogenado, e a sua dependência no tamanho das nanoestruturas, na discussão da celeridade das reações de absorção e desabsorção do hidrogénio. Por fim discute-se como a sensorização pode ser implementada quer durante o regime transitório da hidrogenação quer durante o regime estacionário.

Abstract

From its applications in space aircraft industry fields to the recent advances in the design of fuel cells the role of hydrogen in industry has become increasingly more important over the years. However two of the major issues related with hydrogen is its highly volatile nature and the fact that when mixed with oxygen, namely for concentrations in the range of 4%-74% (v/v) in air, it creates an extremely explosive mixture. Therefore it is crucial to be able to develop cheap hydrogen sensors that are fast enough in the detection of H_2(g) leaks in order to prevent explosions. For that purpose Pd has been one of the most studied materials especially due to its H_2 catalytic and absorbing properties. More explicitly, the ability to break the bond of hydrogen molecule at its surface and incorporate the resulting H atoms into its crystalline structure. Nanotechnology and self-assembly processes allow us to fabricate nanostructured Pd with well-known advantages. Besides reducing hydrogen embrittlement effects when compared with Pd bulk or thin film samples, the nanostructuration also allows to increase the kinetics of the hydrogen absorption and desorption and to explore confinement effects.

The first part of this work (Chapter 2) consisted in the fabrication of Pd Nanowires and dendrites trough the pulsed electrodeposition technique (assisted by anodic alumina templates). It is discussed the specific issues and constrains when electrodepositing Pd through this method and also it is addressed how via a Fabry-Perot light interference phenomena we are able to monitor with the naked eye and in real time the NW´s length and the uniformity of the NW´s growth.

While for the second part of this work (Chapter 3) it is reported the preparation of Pd samples and their functionalization as H_2(g) optical sensors. The sensors response to the presence of H_2(g) were characterized, at room temperature, by performing optical transmissions measurements. We take into account the effects of Pd-Hydride phase transition and its size dependency to explain the kinetics of the hydrogen absorption and desorption in the studied samples. We demonstrate how this sensor can be employed to monitor hydrogen gas concentration either by measuring the rate of signal decay during the Pd hydrogen absorption (transient regime) or by measuring the total variation in signal once the Pd hydride system achieves the equilibrium state (stationary regime).

Contents

List of Tables

List of Figures

Nomenclature

AAO – Anodic Aluminum Oxide

c.p. – Critical Pressure

FCC – Face Centered Cubic

F.P. – Fabry-Pérot

H – Hydrogen

H_2(g) - molecular Hydrogen gas

HILE - Hydrogen-induced Lattice Expansion

NPA – Nanoporous Alumina

NWs – Nanowires

P-C – Pressure Composition

Pd – Palladium

Pd H – Palladium Hydride

PED – Pulsed Electrodeposition

PEM – Polymer Electrolyte Membrane

p.p. – Partial Pressure

SEM – Scanning Electron Microscope

j_{dep} – density current of the deposition pulse

t_{dep} –deposition pulse time duration

V_{dis} – discharge pulse potential

t_{dis} – discharge pulse time duration

t_{rest} – rest pulse time duration

δ_B – alumina barrier thickness

D_p, – diameter of the alumina pore

D_{int} – distance between the neighboring pores alumina

Chapter 1

Introduction

1.1 The role of Hydrogen in the industry

1.1.1 The H_2(g) as the Future energy carrier

Hydrogen is the most abundant chemical element in the universe and since its discovery is has been extensively use by mankind in industry [1]. Its use in petroleum refineries namely in the hydrotreatment of petroleum crude, enables through hydrocracking the conversion of the large hydrocarbons molecules into the common available gasoline, diesel and heating oil. In metal production industry it plays a crucial role, as part of the hydrogen-nitrogen protective and annealing atmospheres, such as the ones used in several types of steel manufacturing [2]. It has been used by NASA for decades as the rocket fuel to deliver its crews and cargo into space, by food and pharmaceutical facilities in hydrogenation process of their products and so on [2-3]. Despite of all these applications, the major impact on the Hydrogen stocks was the recent announcement of H_2(g) as one of the alternatives to fossil fuels for vehicles, mostly due to the latest development of proton exchange membrane (PEM) used in fuel cells [4-6]. Although H_2(g) can also be used in internal combustion engines, the fuel cells can achieve higher energy efficiency of the order of 70%. The fuel cell allow, through the presence of a Pt catalyst and the PEM, to generate electricity through the combination of H_2 and O_2 molecules, as illustrated in Fig 1.1 [9]. Most importantly it has the advantage of having pure H_2O as the only reaction product. Having no trace amount of greenhouse gases emissions, makes the use of H_2(g) (as an energy carrier) a cleaner and environment friendly alternative to the fossil fuels [5]. Although the prior source of H_2(g) is still based on steam reforming of hydrocarbons molecules [6], developments on cleaner approaches, such as the conversion of solar energy into H_2 by photocatalytic water splitting, have reached promissory results that possibilities one day a greener worldwide use of Hydrogen as an energy carrier [7,8].

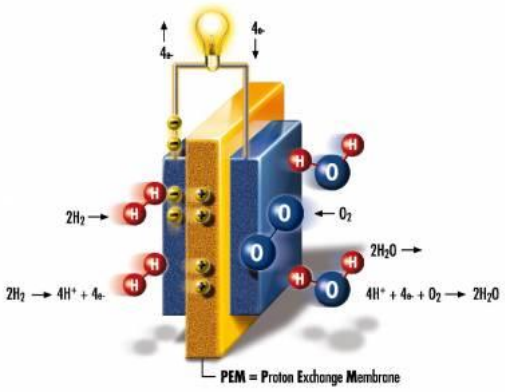

Figure 1.1: Illustration of the mechanism behind the Fuell Cell functioning (taken from Ref [9]). On the right a flow of H_2 (g) reacts with a platinum catalyst. The dissociation of H_2 and adsorption of H atoms occurs. After the ionization of the H atoms at the Pt/PEM interface, the H^+ protons permeate through the PEM which is insulating to electrons. The buildup of the electrons at the interface between the Pt catalyst and PEM leads to a flow of current through the electrical wire. The electrons and H^+ recombine in the presence of oxygen and a catalyst in the left interface to form H_2O.

1.1.2 Safety practical issues in H_2(g) implementation

The H_2(g) storage and transportation still presents practical issues since it is a highly volatile gas and it has a wide range of flammability. When mixed with oxygen, namely for H_2(g) concentrations in the range of 4%-74% (v/v) in air, it creates extremely explosive mixtures. The ignition energy spark is lower than the typical human static spark, with a minimal cost of the order of 0.02 mJ [2]. Also, besides H_2 (g) being an odorless gas, the combustion flames that result from the burning of H_2 and O_2 are nearly invisible to the naked eye, because their emitted light lies mostly within the ultraviolet spectra [11]. This makes a leak or even an H_2(g) based fire harder to notice. Moreover, the ability that H_2(g) has to dissolve in certain metals/crystals, namely in welding junctions, often leads to the fracture of the materials [13-15]. The H_2(g) absorption and desorption results in the successive crystal´s lattice expansions and contractions eventually leading, after several H_2(g) exposures, to the creation of dislocation defects that results in the cracking of the material. This cracks may result in spots for H_2(g) to leak and therefore this not only demands a careful choice of the materials used, for e.g. in H_2(g) storage & transportation structures, but also demands extra safety cares in its implementation.

The development of the fuel cells and the perspective of H_2(g) as the future energy carrier, triggered the search for a new generation of H_2(g) sensors expected to be more reliable, faster and cheaper to produce. Hydrogen sensors are usually needed to monitor the absolute H_2(g) concentration (partial pressure) for process controlling but also to quickly detect H_2(g) leaks in order to prevent explosions [2,12]. As established by the Department of Energy of USA for market placement sensors, safety sensors should be able to detect H_2(g) concentrations below the flammability concentration limit of 4% v/v in less than 1 s, as seen in table 1.

Table 1.1 - The Department of Energy targets for Hydrogen Safety Sensors R&D (from Ref. [11])

Parameter	Value
Measurement Range	0.1% - 10%
Operating Temperature	-30 to 80 ºC
Response time	Under one second
Accuracy	5% of full scale
Gas environment	Ambient air. 10%-98% relative humidity range
Lifetime	10 years
Interference Resistance	e.g. Hydrocarbons

The new sensors are to be incorporated in H_2(g) fuel stations and vehicles but also to reinforce/substitute the already existing ones in the H-industry facilities.

1.1.3 The current market H_2(g) sensors

A variety of mechanisms has already been used for monitoring H_2(g), namely techniques based on gas chromatography (GS), mass and Raman spectroscopy (MS and RS), thermal conductivity and also on solid state sensors whose electrical/optical properties are influenced by the chemical adsorption or absorption of H_2(g) [2]. The GS, MS and RS have a good sensitivity and in fact they can be used for detection of other gases, but are relying on expensive and bulky measurements setups. For that reason they require gas and purge lines to sample air from different locations at a given facility, limiting the speed and also the number of sensing points [2]. On the other hand, the solid state sensors, which include Electrochemical-based Sensors, Metal-Oxide Sensors (MO), Catalytic Bead (CB) and Pd-based sensors, are cheaper to fabricate at an industrial scale through the common micromachining techniques and in few cases they can be individually integrated in the sensing area in order to measure independently and simultaneously H_2(g) in several locations.

The Metal-Oxide and Catalytic Bead sensors rely on heating catalyst to temperatures as high as 100-300ºC to sense H_2(g). Furthermore, in the electrochemical sensors their sensing reactions require the presence of O_2(g) [12]. Due to their high work environment temperatures and the need for the presence of O_2(g) they are unsafe to use when dealing with high H_2(g) concentrations. Palladium (Pd), a functional material for H_2(g) sensing (see section below), has appeared as an alternative option since its hydrogenation is reversible at room temperature and does not require the presence of O_2(g) or heating for H_2(g) sensing [16,17]. Therefore, Pd-based

sensors are the safer option to choose for the detection of H_2(g) leaks or for monitoring high H_2(g) concentrations.

1.2 Palladium as a functional material for hydrogen sensing

Palladium is a transition metal and, as other metals (Ni, Ti, Zi), it has the ability to catalytic dissociate the Hydrogen molecule at its surface and incorporate the resulting H atoms into its crystalline structure [16]. What makes Pd outstand is the fact that it is one of the chemical elements with the highest H solubility and it is also one with the highest functional temperature window range, as observed in Fig. 1.2 [18]. Furthermore the Pd hydrogenation is reversible at room temperature and Pd can absorb large volumes of H up to as 900 times its own volume, reaching atomic ratios of H/Pd as high as 0,67 [4]. The hydrogen catalytic and absorbing properties at room temperature associated with a very low capacity to dissolve other common gases (N_2, O_2, CO_2), qualify Pd as an ideal starting material to develop reliable H sensors and also H purifying membranes [18]

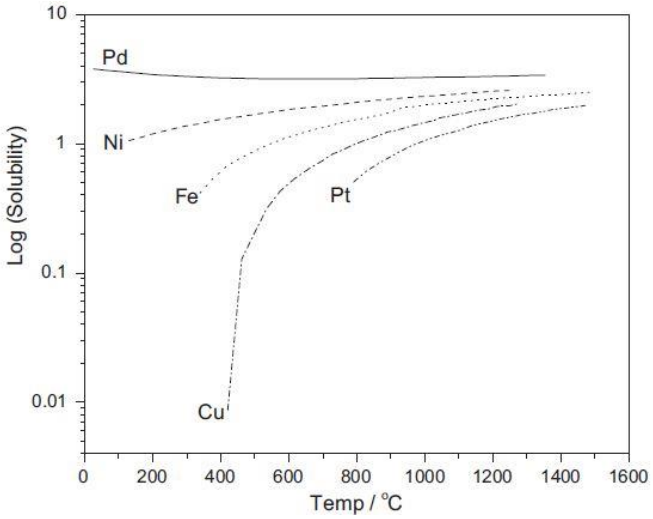

Figure 1.2: Comparison of the Hydrogen solubility for several metals at a pressure of 1 atm. Solubility is given in standard units of cm^3 of H_2 per 100 g of metal (figure taken from Ref. [18]).

1.2.1 The Palladium hydride formation

The palladium hydride formation occurs through several mechanisms, as illustrated in Fig. 1.3. Firstly the hydrogen molecules diffuse through the atmosphere until they reach the Pd surface. Once they are close to it they are physically adsorbed. In others words, the H_2 molecule is kept close to the Pd surface due to an attractive potential resultant of a Van der Waals force [19]. Afterwards through the breaking of the H_2 molecule bond and the establishment of a chemical bond between the H and Pd atoms at the surface, the chemical adsorption occurs. This reaction is exothermic, resulting in a heat release of about 39 kJ/mole [20]. Here the rate of the H

chemical adsorption is thermal dependent due the existence of an energy barrier (E_a) between the physically and chemically adsorbed states, as seen in Fig. 1.3b). This energy barrier is dependent not only on the index of the Pd surface but also on the coverage ratio of the surface defined as the number of H atoms chemically adsorbed per Pd surface unit cell [21]. The rate of hydrogen chemical adsorption can be expressed through the empirical Arrhenius relation, which takes into account the number of free H surface sites (θ_s), the number of physically adsorbed hydrogen molecules (θ_{H2}) and the temperature, expressed by the following equation:

$$r \propto 2\theta_s \theta_{H2} \exp\left(-\frac{E_a}{k_B T}\right) \tag{1.1}$$

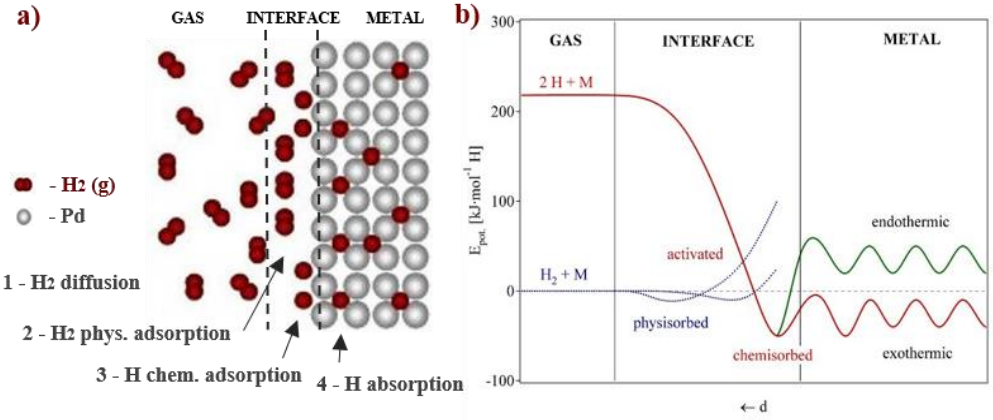

Figure 1.3: a) Illustration of the sequence of the Pd - hydrogen adsorption and absorption process. b) Lennard-Jones (L.J.) potential for H approaching a metallic surface. In the Pd case the typical L.J. potential corresponds to the red line, where the adsorbed and absorbed states are the more energetically favorable states. It is also illustrated that the H occupation sites in the surface and in the first Pd subsurface layer have a lower energy than the interstitials sites within the bulk Pd. This image was adapted from Ref. [20].

Finally, once the H atoms are adsorbed they can diffuse to the interior of the Pd, giving rise to the H absorption. Ab initio studies have shown that the adsorbed state in the Pd surface corresponds to the Pd-H configuration state with the minimum energy. The second minimum energy configuration state corresponds to the occupation of hydrogen atoms at the first Pd subsurface layer [22, 27]. Thus, for low H uptake the H atoms occupy mostly the sites in or near the Pd surface, limiting the ratio of H absorption [21].

Within the bulk of Pd the thermodynamic Pd hydride formation can be described by the typical pressure-composition (P-C) isotherms presented in Fig.1.4.The pressure composition isotherms reveal for a constant temperature the evolution of the H absorption as a function of the H_2(g) partial pressure (p.p.) [16]. At room temperature and for a H_2 p.p. bellow a critical pressure (c.p.) the H atoms are dissolved in Pd as a solid solution. In this phase, also known as the α-phase, the H atoms have a high mobility, with a diffusion constant of 4. 10^{-7} cm^{-2} s^{-1}, the H

atoms behave just like a gas within the metal [23]. As the H_2 p.p. is increased, there is a gradual increase in the H/Pd atomic ratio as well as in the lattice constant from 3.889 Å up to 3.893 Å. This occurs until a 0.015 of H/Pd atomic ratio is reached. For higher H_2(g) pressures and above a critical transition phase pressure, the H atoms start to aggregate in Pd-hydride domains that exhibit a rocksalt type structure [16]. The hydrogen atoms start to occupy the octahedral interstitial sites within the Pd FCC lattice, as illustrated in Fig. 1.5. This phase is known as the metal hydride phase or more commonly known as the β phase [23].

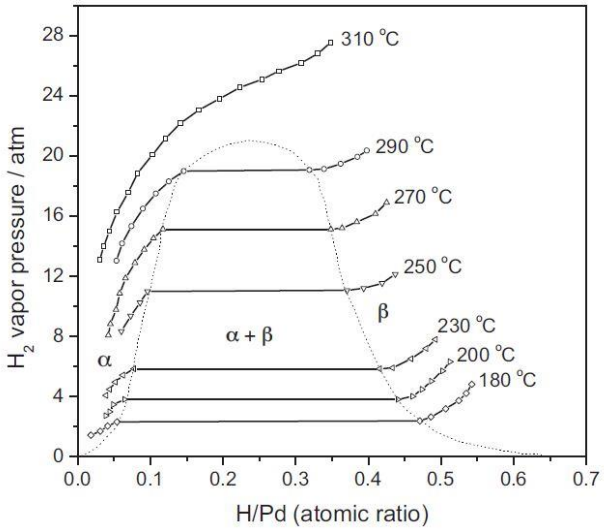

Figure 1.4: Illustration of the typical pressure-composition (-C) isotherm relation for the Pd hydride system at distinct temperatures (taken from Ref. [18]).

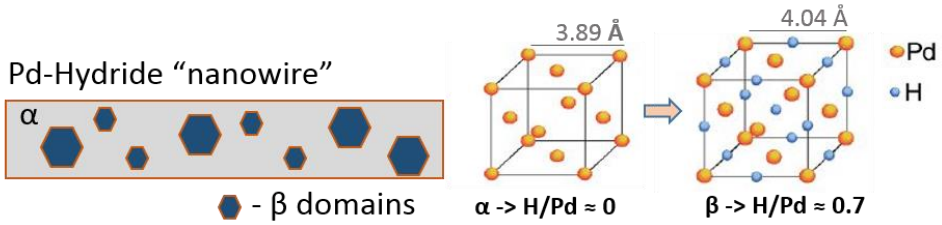

Figure 1.5: Illustration of the nucleation of the β-phase domains within a Pd structure at the left side. At the right side it is represented the expansion of the lattice constant as the Pd hydride transits from the α to β-phases. The octahedral sites for hydrogen occupation are represented by the blues spheres. Crystal representations taken from Ref. [38]

The transition phase between the α state to β state appears in the P-C isotherm as a flat plateau, where a large increase in the atomic H/Pd ratio, from 0.015 to 0.58, is observed for a slight increase in the H_2 pressure [23]. Above this critical H_2 pressure (c.p.) the α-phase disappears and a gradual increment in the H content can be further seen. At room temperature the H/Pd atomic ratio saturates near the value of 0.67 meaning that only 67% of the octahedral sites are occupied by the H atoms. X-ray diffraction measurements show that during the nucleation of the β phase new Bragg peaks are detected, revealing an expansion of the lattice constant up to

4.04 Å [23]. When compared with the lattice constant of the α-phase (3.893 Å), this corresponds to an overall increase in the unit cell volume of 11%. During the phase transition, the coexistence of the two phases usually leads to the formation of dislocations defects due to the lattice misfits. For successive hydrogen exposures this buildup stress eventually leads to the fracture of the Pd structures and their flacking from the supporting substrates. This degradation is known as the hydrogen embrittlement [15].

The transition from α to β-phases is an exothermic process. From the P-C isotherms performed at constant and distinct temperatures, it can be estimated through the Van't Hoff plot a heat releasing of 37.4 kJ/mole [24]. Therefore and although the hydrogen absorption is reversible at room temperature the rate of the H desorption is still dependent on thermal fluctuations. It is also seen that as the temperatures increase, the solubility of the H in the α-phase increases and the width of the phase transition plateau decreases. Also for temperatures higher than the critical temperature of 298 ºC, the abrupt α to β-phase transition disappears and the hydrogen uptake proceeds in a more continuously mode [18].

1.2.2 α to β phase transition and its Pd size dependency

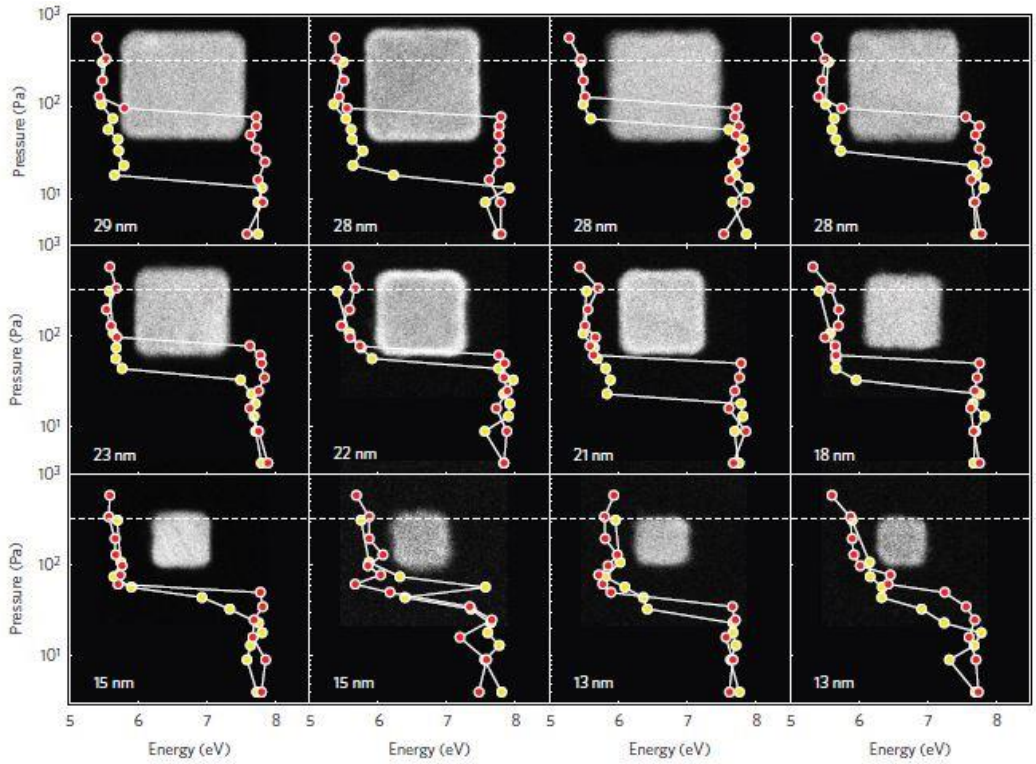

Figure 1.6: Comparison of the P-C isotherms for Pd nanocubes of distinct sizes. The red/yellow dots correspond to Hydrogen absorption/desorption, respectively. The dashed white lines correspond to the critical pressure for the α to β-phase transition in the case of bulk Pd. This figure that was taken from Ref. [25]

Hydrogen desorption measurements, as shown in Fig. 1.6, reveal the existence of hysteresis since the critical pressure for which the β- to α-phase transition occurs is lower than the loading

c.p. measured for the α to β transition. Recent experimental studies, based on the size dependency of the α- to β-phase transition, have shown that the area of the hysteresis as well as the loading critical pressure for the α to β transition decrease as the Pd particles become smaller (Fig. 1.6) [25, 26]. As the hysteresis area decreases the α- to β-phase transition seems to occur in a more continuously fashion. This behavior was also reported previously, where an increase in the maximum α-phase solubility from 0.015 H/Pd to 0.03 H/Pd and a decrease in the β H/Pd atomic ratio from 0.58 to 0.44, when comparing P-C isotherms of 20 μm Pd polycrystalline grains with Pd nanocrystalline grains [27]. This increase in the solubility of H in the α-phase, as the size of the nanoparticles/grains decrease, is recognized as a confinement effect. As the ratio of surface to volume increase, the ratio of subsurface sites (that are associated with a lower chemical potential, as mentioned earlier) to the octahedral sites within the core of the Pd nanoparticles also increase [22, 27, 28]. Thus, a higher H content per Pd mass is achieved before the α-β phase transition takes place inside the core of the Pd nanoparticles.

Figure 1.6 shows that in the range of bulk Pd to 13 nm Pd particles size, the typical flat plateau in the P-C isotherm curve is still observed. However, in another studies reported in the literature, Pd particles with 3.5 nm and 2 nm thick Pd films have shown that the α- to β-phase transition is suppressed [35]. In this size range, it is clear that confinement effects should be more noticeable as the number of surface atoms starts to be approximately equal to the number of core atoms (for e.g. if we consider 2.5 nm cube shaped particles, the ratio surface atoms to core atoms is 0.954). Thus higher deviations from the bulk type behavior are expected. Note that the suppression of the α- to β-phase transition does not depend only on the Pd size, being also observed for Pd alloys bulky samples, namely when doping with Ni, Au for example [2, 19, 44].

1.2.3 Pd-based sensors and the nanostructuration of Pd

The stability of the Pd hydride formation is related to a coupling of the 4d-bands of Pd and the 1-s bands of H [30]. The hydrogen absorption results in a change in the electronic density of states which is reflected by a change in the electrical permittivity of Pd [30,31]. Consequently, this can be measured through a variation of the electrical conductivity or the refractive index ($\tilde{n}$), as observed in Fig. 1.7 [31,32]. Several transducers have been designed to monitor H_2(g) concentrations through these changes. In this subsection, we will describe some current types of Pd sensors, distinguishing between the resistive and optical ones, and remark the benefits that nanotechnology has to offer to their performance.

1.2.3.1 Pd-based resistive sensors

The resistive sensors work is based on the change of resistance during the H absorption and its response is dependent on the type of structures used. In the case of continuum Pd, such as thin films or single nanowires [Fig. 1.8 a)], the sensor response is determined by the increase of resistivity as the transition from Pd to Pd-hydride occurs [Fig. 1.8 b)] [33-35]. For other types of configurations such as discontinuous Pd, such as Pd films grown in Volmer–Weber mode (islands) or even Pd nanoparticles or nanowires embedded in films [Fig. 1.8 c)], the response is manly determined by the hydrogen induced lattice expansion (HILE). More explicitly, since the hydrogen absorption leads to an increase of the Pd lattice constant, the increase in volume of each Pd nanostructure leads to the establishment of extra electrical paths between the neighboring nanoparticles, leading to a decrease in the electrical resistance, as illustrated in Fig. 1.8 d) [35-37].

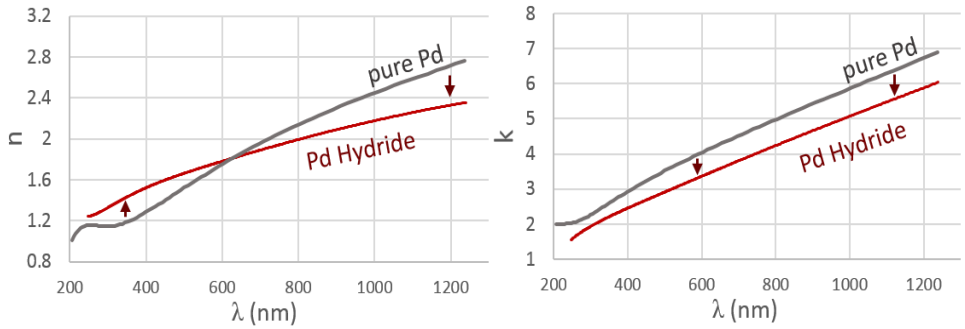

Figure 1.7: Variation of the refractive index of Pd upon hydrogenation (ñ = n +ik). The data was extracted from Ref. [31]. It was obtained through ellipsometry measurements of a 12-nm-thick Pd film deposited on quartz substrate when exposed to 1-bar hydrogen, well above the transition c.p.

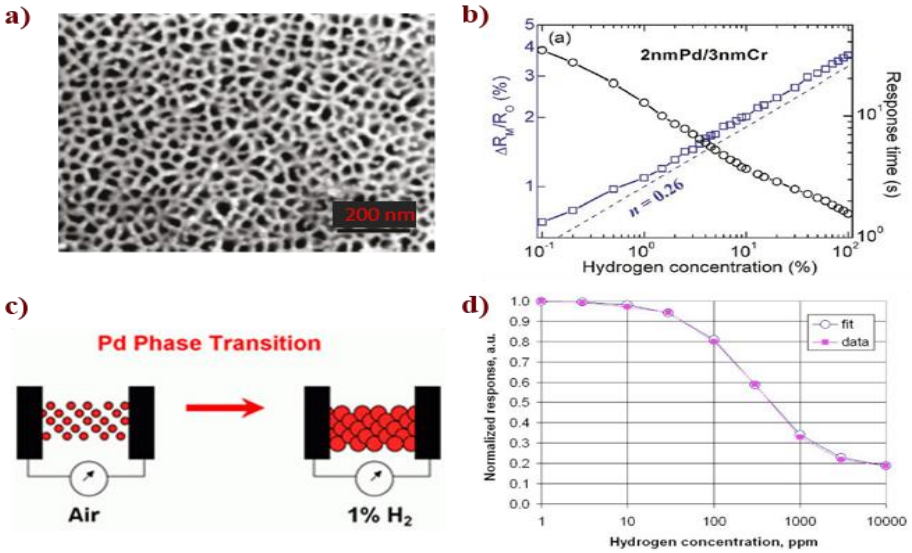

Figure 1.8: Resistive Pd Sensors - a) Continuous 2 nm Pd thin film sputtered on the top of a nanoporous alumina template and b) its response to H_2(g) concentrations of 0.1 to 100% v/v in air. (figures taken from Ref. [36]) c) Pd nanoparticles with 35 nm embedded in a thin film and d) its response through HILE effect for a H_2(g) concentration of 0.1 to 5% v/v in air. (figures taken from Ref. [37])

However, the use of these kind of measurement setups present risks when dealing with high H_2(g) concentrations. These electrical circuits can generate electrical sparks that could be responsible by the ignition of H_2(g) explosions. Therefore, the development of optical sensors has appeared as a more logical and safer alternative, since through the use of optical fibers it is possible to use remote light sources and detectors, excluding the necessity of using electrical connections in the sensing area.

1.2.3.2 Pd-based optical sensors

The hydrogen absorption as measured by Isidorson (Fig. 1.7) affects both the real and imaginary parts of the optical refractive index (ñ) [32,38]. Several techniques based on the use of either Pd claddings or micro mirrors in optical fibers have exploited this effect to monitor H_2(g) [39]. For example interferometry measurements relying on the change of refractive index either of Pd as well of the fiber´s core due to elasticoptic effects, since the fiber is submitted to strain as the Pd cladding expands due to HILE. The latter effect can also be used to sense H_2(g) in fiber Bragg/long period gratings. Another approach could be by simply measuring the change in light absorption as the evanescent field of the fiber´s mode interacts with the Pd cladding during hydrogenation [40]. One of the major issues in these measurement setups is that after several hydrogen exposures the Pd films flakes from the fiber due to hydrogen embrittlement [41]. Also within the field of optical hydrogen sensors and in order to enhance sensitivity, sensors based on the excitations of localized surface plasmon resonances have been developed based on Au-Pd and Ag-Pd systems. Also within the field of optical hydrogen sensors and in order to enhance sensitivity, sensors based on the excitations of localized surface plasmon resonances have been developed based on Au-Pd and Ag-Pd systems. In this case, the Pd-hydride system is used as a surrounding changing index medium that shifts the resonance frequency of the plasmon excitation in the Au/Ag structures [42,43]. Several configurations have been explored, from Au-Pd cladding of optical fibers to Pd-Au films stripes, as depicted in Fig. 1.9 a) and 9 b) respectively. Also more recently in the form of nanostructured Au-Pd sensors, as in the system of core-shell nanowires depicted in Fig. 1.9 c), or even on AuPd alloy nanodiscs [Fig. 1.9 d)] [41-44]. The major drawback is that they typically rely on high cost nanofabrication techniques, namely photolithography and high vacuum deposition systems.

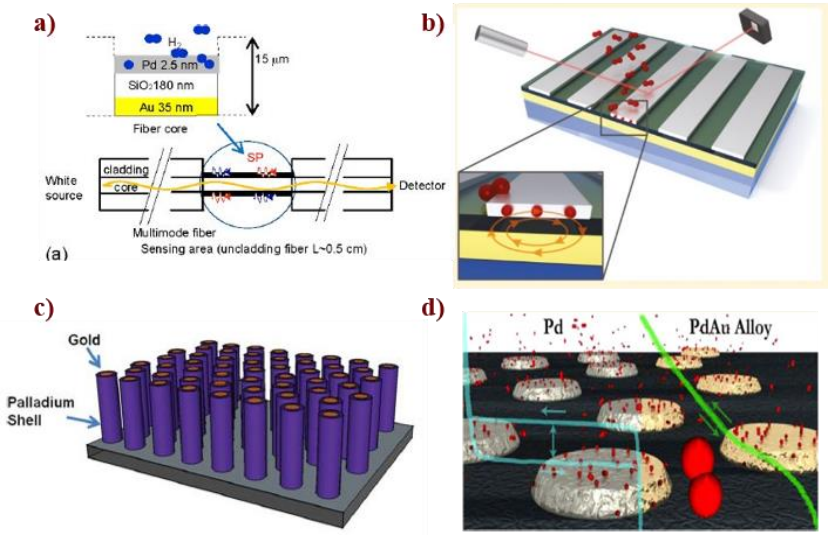

Figure 1.9: Optical sensors based on the excitations of plasmons in several configurations. a) Optical fiber with cladding of Au and Pd thin films [41]. b) Pd stripes and Au thin films [42]. c) Core-shell Au-Pd nanowires [43]. d) Nanodiscs consisting in alloys of PdAu [44].

1.2.3.3 The benefits of the Pd nanostructuration for H_2 sensing

Under the performance of the Pd solid state sensors, either employed as an optical or restive transducer, always underlies the thermodynamics of the H absorption and desorption. The use of nanostructured Pd, as mentioned above, has obvious advantages. The increase of the surface to volume ratio but also the lowering of the enthalpy of the β Pd-hydride formation, as the Pd size structures get smaller, allows to increase the kinetics of the hydrogen absorption and desorption at room temperature [19]. This enables the development of faster sensors and also allows, when compared with Pd bulk or Pd thick film samples, to reduce hydrogen embrittlement effects [16]. As discussed earlier, since the maximum H/Pd atomic ratio increases in the α-phase and the minimum H/Pd ratio of the β-phase decreases as the Pd size decrease, this allows to reduce the lattice misfit during the coexistence of the two phases and therefore to minimize the formation of lattice dislocations defects. Enabling for that reason to extend the life time of the sensors [2]. Moreover, a further decreasing in Pd size until the α to β transition is suppressed, enables to extend the range of detection of hydrogen [35]. In the case of embedded 35 nm Pd nanoparticles, as observed in Fig. 1.9 d), the sensor is unable to distinguish H pressures higher than the critical pressure since the H/Pd atomic ratio tends to saturates near 0.67 [37]. At room temperature this corresponds in a saturation of the signal response near 4% of H_2(g) in air (v/v). On the other hand, as we explore further the confinement effects, as in the case of 2 nm thick Pd film [Fig. 1.8 a) and 8 b)], the sensor is able to distinguish H_2(g) concentrations up to 100 % due to the suppression of the α to β transition [35]. Similar

results are reported for PdNi resistive films or in the AuPd nanodiscs used as optical plasmonic sensors [Fig. 1.10 d)]. Due to chemical alloying the destabilization of the β hydride formation also enhances the sensor performance as it also reduces the area of hysteresis of the Pd hydride p-C isotherms enabling to decrease the sensor uncertainty [44].

1.3 Pulsed electrodeposition in nanoporous alumina templates

In order to fulfill the low cost requirements for the market integration of new Hydrogen sensors, the most logical approach for developing nanostructured Pd H_2(g) sensors relies on the use of self-assembly fabrication techniques. Pulsed Electrodeposition (PED) assisted by anodic alumina templates, as reported by Nielsch, is an industrial friendly technique that allows in an accessible way to fabricate metal nanowires and dendrites [45,52,56,57,58]. Since 1995 and thanks to Masuda group, it was reported that the controlled mild electrochemical oxidation of an Aluminum (Al) foil results, through a self-assembly process, in the formation of organized nanoporous alumina (NPA) templates, that can be used as a mold to grow metal nanowires. More recently NPA samples as large as 14x14 cm^2 have been successfully grown [50].

1.3.1 Anodic alumina templates

The self-assembly process is driven by an oxidation rate of the Al surface and also a local dissolution of the alumina in the electrolyte/alumina interface, from which results the growth of the alumina pores in depth, as illustrated in Fig. 1.10 [46-49]. A two-step anodization process developed by Masuda is usually performed to achieve higher organizations. After growing a first sacrificial NPA template and after its chemical removal, a 2nd anodization is performed at the same conditions (discussed in more detail in the experimental section of chapter 2).

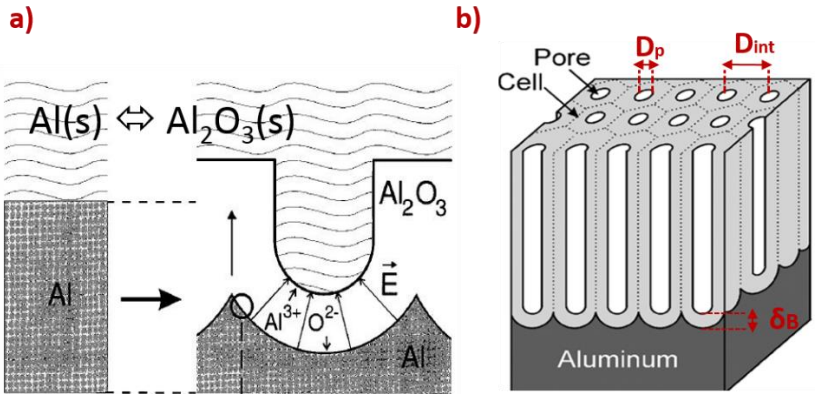

Figure 1.10: Illustration of the aluminum anodization process and the schematic representation of the structure of nanoporous alumina template. Image adapted from Refs. [48] and [50].

The geometry of the NPA templates is characterized by several parameters such as the diameter of the pores (D_p), the distance between the neighboring pores (D_{int}) and also the alumina barrier

thickness between the bottom pores and the Al substrate (δ_B). These parameters are dependent on the anodization conditions such as the type and temperature of the electrolyte bath and also on the applied voltage (V_a). For a 0.03 M Oxalic acid the empirical relations are observed [49]

$$D_{int} = 2.5\, V_a\ (nm/V) \tag{1.2}$$

$$D_p = 0.7\, V_a\ (nm/V) \tag{1.3}$$

$$\delta_B = 1.3\, V_a\ (nm/V) \tag{1.4}$$

1.3.2 The pulsed electrodeposition

Once the NPA template is formed there are three possible electrodeposition methods to choose to perform the metal-filling. The direct current (DC), the alternate current (AC) and the pulsed electrodeposition (PED) [55,59]. At the end of the Al anodization an alumina barrier (an electric insulator) still remains between the bottom of the pores and the Al substrate. In the case of DC electrodeposition, the insulator barrier needs to be removed. Therefore, in order to expose the alumina pores and to establish the electrical connection between the cathode and the later electrolyte, the removal of the Al substrate and of the alumina barrier is firstly performed, typically through a chemical etching, as illustrated in fig. 11 a). Once the pores are fully exposed, an Au film is then sputtered on one side of the NPA template. In this way, it is deposited at the bottom of the pores an electrode that is able to transfer electrons to ions of a given electrolyte if an external voltage is applied, enabling the growth of Pd nanowires [58,59]. However, as the alumina template is brittle and fragile to manipulate on its own and since this protocol involves removing its supporting substrate, this protocol is hard to implement at an industrial scale [45, 56]. For this reason, we have decided to use the PED process as it relies on a simpler and relatively easier/cheaper fabrication process. As mentioned before, at the end of a standard anodization, when using the oxalic acid electrolyte and an applied voltage of 40 V, a 51 nm insulating alumina barrier remains at the bottom of the pores and the Al substrate. By proceeding with an non-steady anodization process, in which the applied voltage is decreased exponentially in time from 40 V down to 2-14 V, it is possible to reduce and tune the alumina barrier to a thickness small enough to allow the passage of an electric current through the tunnel effect (eq. 1.4) [54]. This thinning of the barrier enables to transfer an electron current pulse through the barrier to reduce the complexed ions to atoms and therefore to grow nanowires. Moreover during the non-steady anodization process the diameter of the alumina pores also decrease according to eq. 1.2. Due to the formation of electrical instabilities, this leads to pores

division and consequently the formation of several Y pore structures that are known as the dendrites, Fig. 1.11b) [53-55].

The PED method consists in applying cyclically a deposition pulse followed by an alumina barrier discharge pulse and also a rest time interval [45,52,56,57,58]. During the first pulse a constant electric current tunnels through the alumina barrier to reduce, in our case, the Pd ions that are inside the pores to metal. Whereas in the second pulse a constant voltage of inverse polarity is applied to discharge the alumina barrier and therefore to interrupt the deposition pulse. At the first cycles it allows to repair defects in the alumina barrier [58]. The rest pulse that makes PED outstand from the AC electrodeposition method, consists in a waiting time interval. This allows for the ions to diffuse from the bulk electrolyte to the inside of the pores and to reestablish the ionic concentration inside the pores after each deposition pulse [45, 56]. This ensures a higher efficiency of the consecutive deposition pulse and also allows to reduce hydrogen evolution issues [45]. Therefore, the PED appears as an industrially appealing approach to the fabrication of Pd nanostructures, as it enables to grow metal nanowires directly onto aluminum foils just right after performing a potentiostatic and also a non-steady state anodization process.

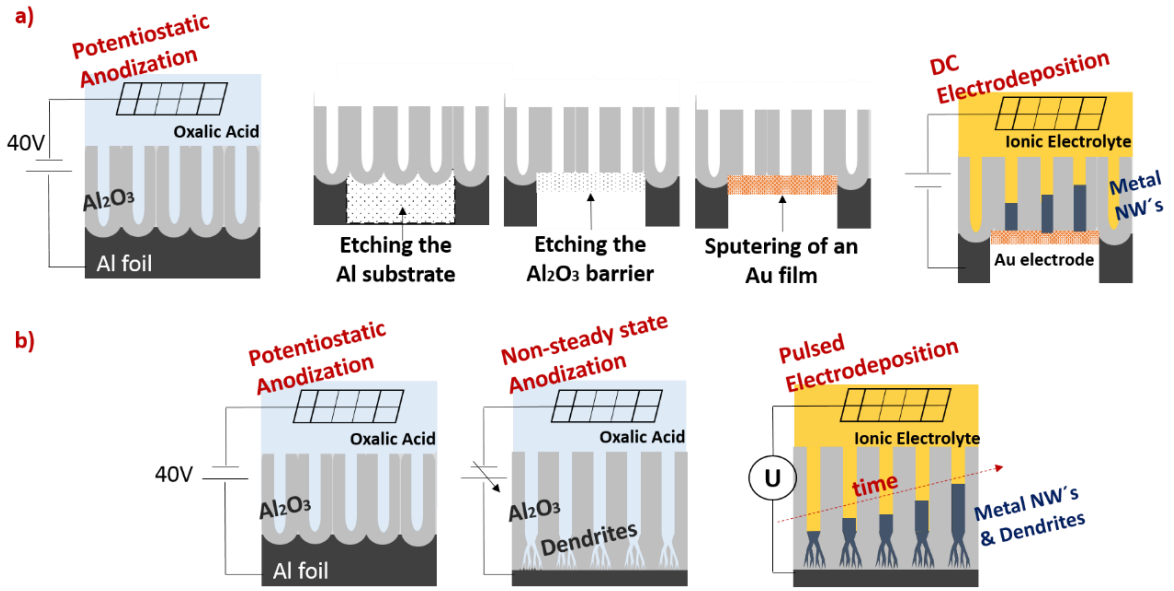

Figure 1.11: Schematic representation of the steps involved in the fabrication of nanowires. a) DC electrodeposition method, partial removal of the Al substrate and Al_2O_3 barrier layer, and the Au electrode coating. b) AC or PED electrodeposition method, through the thinning of the alumina barrier and the dendritic pores formation.

Chapter 2

Fabrication of Pd NWs and Dendrites: Experimental details

The following experimental work was developed at the Alumina´s Lab of IFIMUP-IN. In this chapter it is described the protocol followed during the fabrication of Pd dendrites/NWs through PED assisted by AAO templates. It is discussed the specific issues and constrains when electrodepositing Pd through this technique. It is also discussed how via a Fabry-Perot light interference phenomena we are able to monitor with the naked eye and in real time the NW´s length and the uniformity of the NW´s growth at a macroscopic scale.

2.1. Aluminum Anodization

2.1.1. Samples Preparation - Cleaning and Electropolishing

Initially Al samples of 1.5 x 1.5 cm^2 were cut from Alfa Aesar high purity (99,997%) Al foils. In order to clean and degrease the samples from possible fabrication residues, they were submitted to ultrasonic agitation in acetone and subsequently in ethanol for a period of 5 min each. Since the electrical field lines tend to be concentrated near surface topography irregularities and as the anodization process of the Al surface is driven by an applied electrical field (coulomb attraction of O^{-2} ions species), it was firstly performed an electropolishing of the Al samples in order to ensure an uniform growth of the AAO template [59]. In this process the Al samples were used as anodes and a Pt mesh as a cathode, both were submerged in a $HClO_4$:C_2H_5OH (4:1 v/v) bath solution while applying a voltage of 20 V for a period of 2 min. Since the electropolishing attack is also driven by the electrical field, this polishing is enhanced near the Al surface topography irregularities. This process allows to smooth the surface irregularities and to reduce its roughness [59]. The initial light diffuse reflection of the Al samples is replaced by a specular reflection, resulting in mirror-like surface samples. Afterwards the samples were rinsed in ethanol and deionized water.

2.1.2. Potentiostatic anodization of the Al samples – the two-step anodization process

The two-step anodization process was employed for the fabrication of the anodic aluminum oxide (AAO) templates. The potentiostatic anodization of the Al samples were performed according to the experimental setup illustrated in Fig. 2.1. The Al samples were again used as anodes and the Pt mesh as a cathode, in a 0.3M Oxalic acid ($C_2O_4H_2$) aq. solution while applying a voltage of 40V (V_a). The Al sample was fixed under pressure by means of a O-ring rubber seal. This allowed to fix the sample but also to seal the anodization cell in order to prevent electrolyte leaks unto the copper plate. The anodization cell was kept in a cooling plate in order to maintain the temperature of the oxalic bath close to 3ºC. Stirring was also used to renovate the oxalic electrolyte near the Al sample as well to remove H_2(g) bubbles formed at the Pt grid [48]. An home-made LabVIEW interface program was used to control a Keithley 2400 power supply, working as a voltage source and a current meter at this stage (S). As the external voltage V_a was applied, the density current $j(t)$ flowing through the electrical circuit was measured in order to monitor the anodization process.

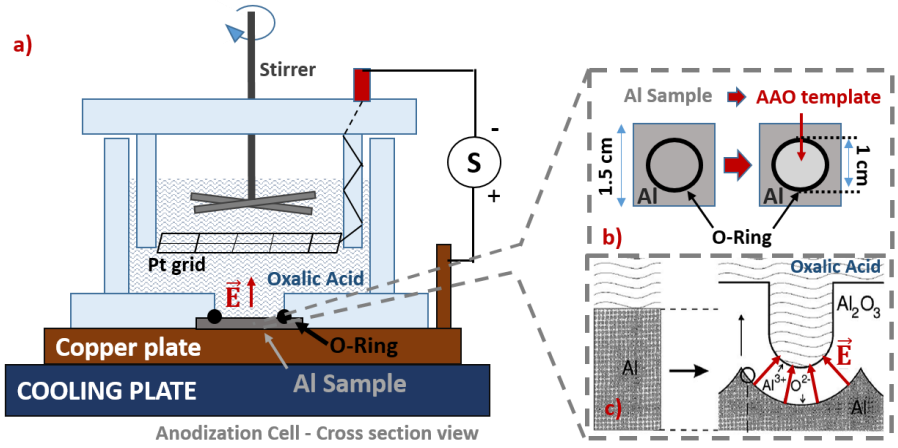

Figure 2.1: a) Experimental setup: cross section view of the anodization cell; b) Geometry and dimensions of the Al sample and of the grown AAO template; c) Illustration of the anodization of the Al foil, highlighting the ion O^{2-} migration through the Al_2O_3 barrier unto the positively charged Al surface. Adapted from Ref. [50]

According to the two-step anodization process, schematically represented in Fig. 2.2, after growing a first sacrificial AAO for 24 h, the resulting AAO templates were chemically removed by submerging the samples in an aq. solution of 0.4 M Phosphoric acid and 0.2 M Chromic acid for a period of 12h at 40ºC. Subsequently a 2nd anodization was performed at the exposed Al surface. The typical measured current density, $j(t)$, of the two anodizations are presented in Fig.2.3. We observe that we are able to distinguish the several stages of the anodization and in

this way to monitor the anodization process. Moreover, the effects of using the two-step anodization protocol on the anodization curves, $j(t)$, are clearly observed [48, 49].

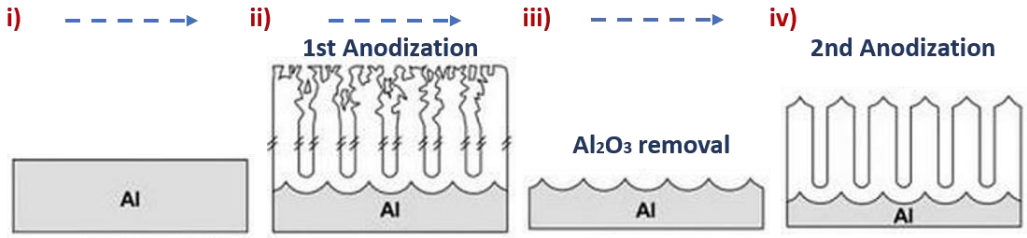

Figure 2.2: Schematic illustration of the two-step anodization process. The preserved hexagonal indentations on the Al foil, obtained after the removal of a 1st sacrificial AAO template, are used as a mask to grown a perfectly organized AAO template. Image adapted from Ref. [48]

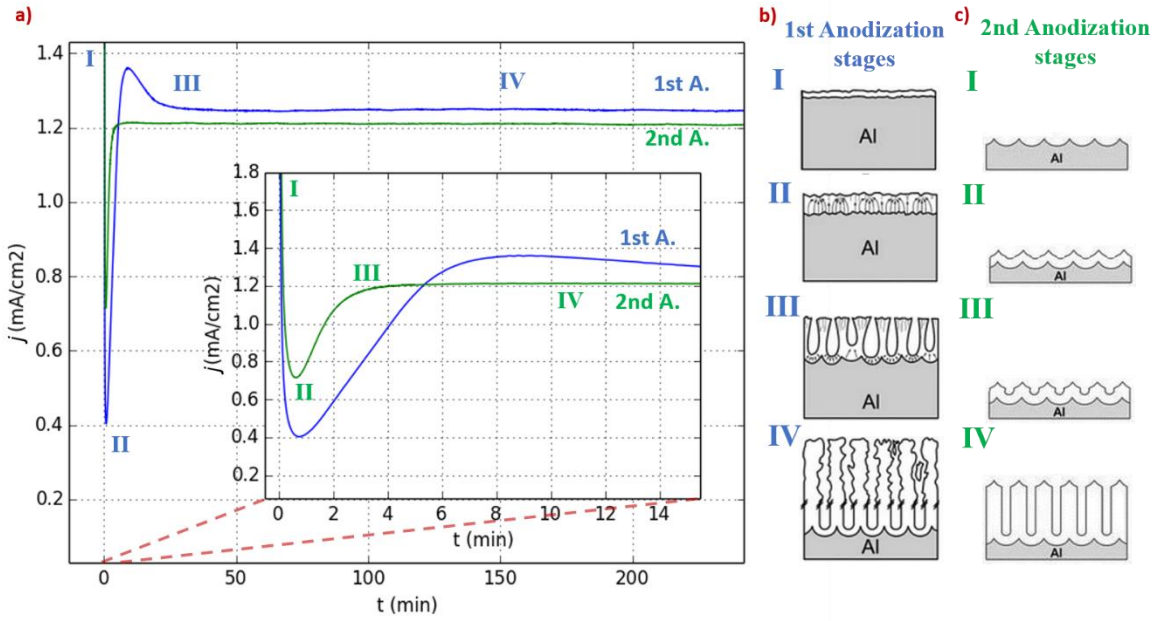

Figure 2.3: a) Comparison of the anodization curves, $j(t)$, for the 1st and 2nd anodizations, using an applied voltage of 40 V in a 0.3M Oxalic acid aq. solution. The inset graph corresponds to a zoom on the time scale. The roman numbers enumerate the different stages of the self-assembly anodization process illustrated on the right columns - b) and c) correspondent to 1st and 2nd anodization, respectively. The AAO template illustrations were adapted from Ref. [48]

The anodization curves, $j(t)$, follow the usual behavior of the mild anodization process [48,49]. At the beginning of the 1st anodization (blue curve), when the Al surface is still exposed, the resistance offered to the ionic current is low, resulting in an initial $j(t)$ of ~ 25-35 mA/cm^2**.** In the following instants, in the I-II stage sequence, as the anodization proceeds the Al foil starts to be covered by an Al_2O_3 film, leading to an increase of the electrical resistance and causing the current density, $j(t)$, to drop until it reaches its minimum value. At stage II the current starts to rise as a result of the self-assembly process [46]. Since the density of the Al_2O_3 film is higher than the Al film, the mechanical tension between neighboring Al_2O_3 nucleation points leads to deformations of the Al_2O_3 film, as shown in Fig.2.3 b)-I. The $O^{2-}_{(ox)}$ ions's diffusion through

the Al_2O_3 barrier is driven by the electrical field (***E***). Therefore the regions where its intensity is higher corresponds to the points where the ionic current flows primarily, as illustrated in Fig.2.3 b)-II. The nucleation's paths for the growth of the pseudo-pores are established in this way [49]. The thermal dissolution assisted AAO growth model describes that these localized ionic current paths induce a local increase in the electrolyte temperature through the Joule effect that promotes a partial dissolution of the recently formed Al_2O_3, namely in the interface between of the Al_2O_3 barrier and the electrolyte [48]. As the local dissolution of the Al_2O_3 progress, the local thickness of the Al_2O_3 barrier decreases, reducing the total electrical resistance. This is observed as an increase in $j(t)$, during the II-III stage sequence. The pseudo-pores grow into the Al foil due to a balanced oxidation and dissolution-rate,as illustrated in Fig. 2.3 b)-III. The initial distribution of the pseudo-pores is not well organized, therefore, as the pseudo-pores grow they eventually merge with neighboring pores or even remain behind, as shown in the schematic Fig. 2.3 b)-III. This competitive behavior is responsible for the local maximum of $j(t)$ seen in stage III. By proceeding with the anodization and through this competitive self-organization process, the pseudo-pores growth eventually reaches the equilibrium. At this stage, they proceed to grow straight and parallel to each other and a constant $j(t)$ is measured (stage IV). Through this self-assembly process, at the end of a 24 h anodization period the bottom of the AAO template, unlike its top, is well organized (Fig. 2.3 b)-IV) [48].

After chemically remove the AAO template, the exposed Al substrate is patterned with a hexagonal matrix of indentations produced by the AAO bottom tips (Fig. 2.3 c)-I). Once the 2nd anodization is performed, these well-arranged indentations assist as a mask to establish the nucleation's paths for the growth of the pores [46]. This behavior is masked in the response of $j(t)$ curve (green curve). Since there is already a predisposition for the organized growth of the AAO pores, the Al_2O_3 partial dissolution and the consequent pores growth begins earlier (sequence II-III). This is detected through differences in the minimum of $j(t)$. It is attained faster and its value is higher than the obtained in the 1st anodization (blue curve). Also, the anodization curve, $j(t)$, tends to its steady-state value (IV) without any bump (maximum), as there is no longer any competition between pseudo-pores in the 2nd anodization because the distribution of the pores growth is well defined from the beginning [46]. Still a slight variation of $j(t)$ in stage IV can be seen but mainly due to fluctuations of the electrolyte temperature. In this way, the two step anodization process allows to obtain a well organized AAO template from its top to its bottom [46]. In Fig. 2.3 below it is displayed micrographs of the resulting AAO templates, obtained by scanning electron microscope (SEM) at CEMUP.

The acquisition of the SEM micrographs was performed at CEMUP by using a high resolution FEI Quanta 400FEG scanning electron microscope. Since the AAO template is an electrical insulator, the measurements were performed under a low vacuum in order to reduce charging effects at the AAO surface. From a statistical analysis of the obtained top view micrograph, performed with the software ImageJ, we obtain an average pore diameter of 40.4 +/- 3.3 nm and an average interpore distance of 115.9 +/- 2.31 nm. This results in a porosity of 11% for the AAO template, close to the expected 10% natural porosity. If we look further to the top view of the AAO template presented in Fig. 2.4 a), we observe the well-defined hexagonal pores array confined to domains of the order of 1 μm size [48]. This multidomain character of the AAO template is clearly shown if we compare the 2-dim fast Fourier transformation (FTT) obtained for the complete micrograph, with the FFT obtained when sampling a localized monodomain [inset of Fig. 2.4a)].

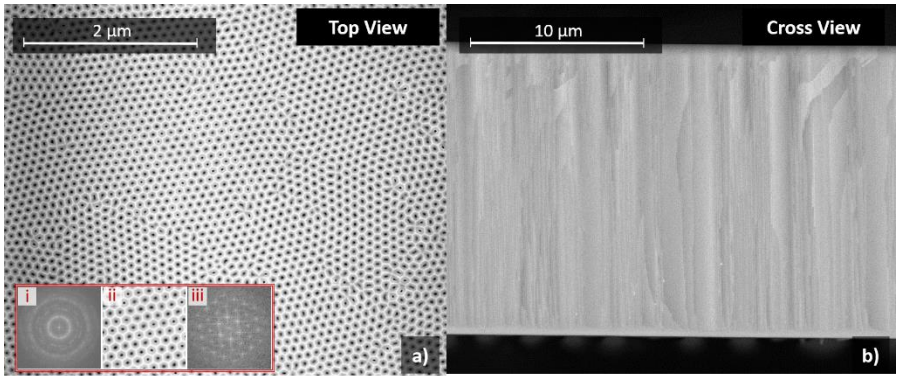

Figure 2.4: Micrographs obtained by SEM of the grown AAO template. a) Top view exhibiting the hexagonal arrangement of the grown AAO pores. At the inset it is shown the respective 2-dim FFT i) and a zoom on a particular AAO monodomain ii) and the corresponding FTT iii). b) Cross sectional view of the AAO template obtained after its mechanical cleavage.

2.1.3. Non-steady anodization – Alumina barrier thinning and the dendrites formation

The Al_2O_3 barrier thinning was performed by a non-steady state anodization process after the 2^{nd} anodization [53,54] . The applied anodization voltage, V_a, was exponentially decreased in steps from the initial 40 V to 8 V. From eq. 1.4, we expect a final alumina barrier thickness (δ_B) of approximately 10 nm [54]. Figure 2.5 presents the response of $j(t)$ during the non-steady anodization.

For each step in the applied voltage V_a(t), we observe a first abrupt decrease in $j(t)$, which is expected since the oxidation rate is driven by the ion O^{-2} coulomb attraction to the Al surface.

After the first fall down, the unbalanced Al_2O_3 dissolution rate leads to a gradual decrease in the thickness of the alumina barrier (δ_B). This results in the continuous decrease of the resistance

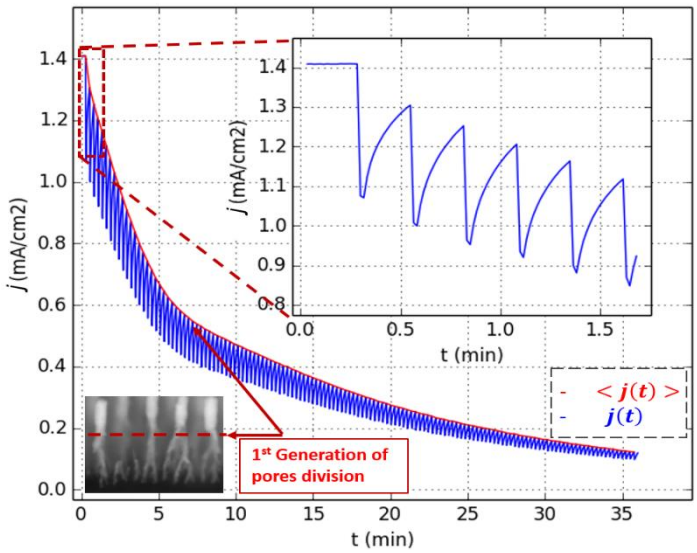

Figure 2.5: Behavior of the density current, j(t), during the non-steady state anodization. The inset graph corresponds to a zoom on the temporal scale. The inset micrograph corresponds to the dendritic pore structure obtained by SEM after performing a Pd electrodeposition.

for the O^{-2} ions migration through the barrier, which can be seen as the observed gradual increase in $j(t)$. Before $j(t)$ achieves its steady-state value, for the transitory applied V_a(t), the applied voltage decreases once more and the above described behavior begins again. In this way the thickness of the alumina barrier (δ_B) as well as the diameter of the pores are reduced [54,55]. Due to the diameter of the pores reduction, the formation of electrical instabilities leads to the pores division [54]. This phenomenon disturbs the rate of decay of the average density current $< j(\mathrm{t}) >$ (red curve of Fig. 2.5). This rate of decay follows the exponential voltage decay but it is attenuated after the first initial 6 min. This stage corresponds to the first generation of pores division [49]. The division of the pores leads to an increase of the effective surface area (higher porosity) and therefore to a decrease in the electrical resistance (R), attenuating the average current decay [j(t) = V_a(t)/R(t)]. Once the desired final voltage (8 V) is achieved, the anodization is prolonged for 3 min to ensure a uniform thickness of the alumina barrier across the entire sample. In the inset of Fig. 2.5 it is shown the obtained dendritic structure after performing a Pd electrodeposition.

2.2. The pulsed electrodeposition (PED) of Pd

In order to perform the PED electrodeposition after the non-steady state anodization, the oxalic acid solution was removed from the anodization cell and substituted by a Pd ionic based one. A distinct LabVIEW interface was used to control the power supply, here used both as a current

and voltage source meter. The LabVIEW interface allow to define the density current that should be applied during the deposition pulse (j_{dep}), the value of applied voltage during the discharge of the alumina barrier (V_{dis}) as well as the duration of each pulse t_{dep}, t_{dis}, t_{rest} (Fig. 2.6).

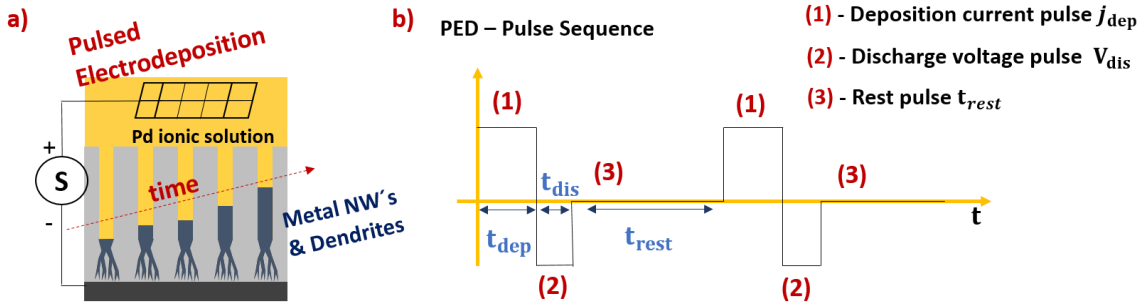

Figure 2.6: a) Illustration of the experimental electrodeposition setup and the sequential filling of the dendritic and AAO main pores; b) Representation of the pulse sequence applied during the pulsed electrodeposition.

First, the source meter works as a current source. To keep constant the selected j_{dep} during the deposition pulse, the source (S) applies the necessary voltage to the electrical circuit. During this pulse, a tunnel current flow through the barrier layer allows for the reduction of the Pd ions forming the dendrites and finally the NWs. If the Pd ion concentration at the bottom of the pores is not enough to allow the current, an electric field is created (capacitor effect) which attracts the ions and increase again the concentration. [56]. In order to monitor the electrodeposition, the necessary applied voltage, V_{dep}(t), is measured during the deposition pulse. In the same way, during the Al_2O_3 barrier discharge pulse (second pulse), as the discharge voltage (V_{dis}) is applied, the resulting current, I_{dis}(t), is measured. This pulse stops the deposition step. Finally, a resting pulse is performed to allow for the diffusion of Pd ions inside the pores restoring the initial concentration. By the continuous repetition of these pulses, the dendrites and the pores are filled from the bottom to the top with Pd metal.

Table 2.1 - The prepared electrolytes for the pulsed electrodeposition of Pd.

Electrolytes	Composition	Pd ionic concentration	pH
1	$Pd(NO_3)_2.H_20 + 4NH_4Cl$ [1:4]	0.0085 M	≈ 2.5
2	$PdCl_2$	0.004 M	≈ 7

2.2.1. Palladium(II) nitrate dehydrate ionic solution

Two kinds of Pd electrolytes were prepared and used in the experimental work (Table 2.1), both based on solutions used in the DC electrodeposition of Pd NW´s [60,61]. Based on the work of

the author Nevin Taşaltın, it was firstly prepared a Pd ionic solution consisting in 0.0085 M Palladium(II) Nitrate dehydrate and 0.034 M Ammonium Chloride aq. solution.
This resulted in an acid solution of pH ≈ 2.5. This was prepared in order to achieve the formation of complex $PdCl_4^{2-}$ ions, as expressed in the following ionic equations:

- $Pd(NO_3)_2.2H_2O_{(s)} + 4NH_4Cl_{(s)} + 4H_2O_{(l)} \rightarrow [Pd(H_2O)_6]^{2+}_{(aq)} + 2NO^{3-}_{(aq)} + 4[NH_4]^{+}_{(aq)} + 4Cl^{-}_{(aq)}$
- $[Pd(H_2O)_6]^{2+}_{(aq)} + 4Cl^{-}_{(aq)} \rightarrow [PdCl_4]^{2-}_{(aq)} + 6H_2O_{(l)}$

During the deposition pulse, the electrodeposition of Pd(s) at the AAO pores is achieved by the reduction of the $[PdCl_4]^{2-}$ complex ions [60], as stated in the following equation:

- $[PdCl_4]^{2-}_{(aq)} + 2e^- \rightarrow Pd^0_{(s)} + 4Cl^-_{(aq)}$

2.2.1.1. The influence of the j_{dep} on the Pd electrodeposition

In order to test the 0.0085M $Pd(NO_3)_2.2H_2O$ electrolyte for the PED method, different electrodepositions were performed for several applied deposition current densities, j_{dep}, ranging from 70 mA/cm^2 to 15 mA/cm^2. A duration of 8 ms for the deposition pulse, a discharge pulse of 8 V and 2 ms duration, as well a 0.7 s rest pulse were commonly used as the remaining parameters. The depositions were performed at room temperature in ~ 2.5 µm thick AAO templates.

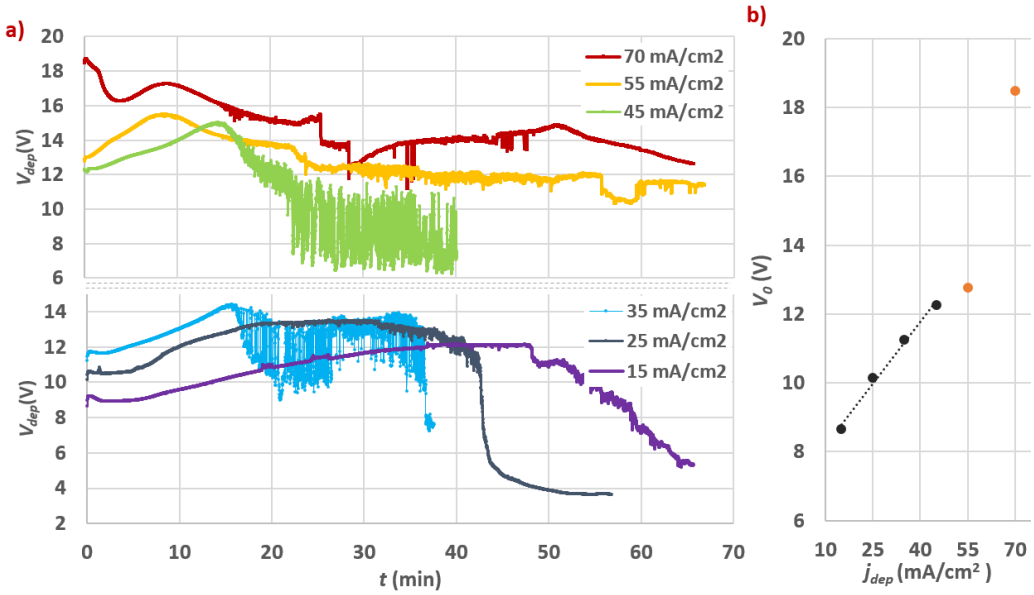

Figure 2.7: a) Representation of the deposition profiles, V_{dep}(t), for several j_{dep}; b) Dependence of the measured voltage at the 1st deposition pulse (V_0) with the applied j_{dep}.

In Fig. 2.7 it is shown the measured deposition V_{dep}(t) curves for each j_{dep}. In the range of 15-55 mA/cm^2, we can see that the voltage typically rises until a given moment, after which it

starts to decrease. The global behavior of these curves can be better understood by treating the overall system by its electrical equivalent circuit [52]. As illustrated in Fig. 2.8, the electrodeposition setup can be interpreted as a series circuit, composed by the resistance of the electrical contacts, including the Al substrate (R_{Al}), of the AAO template and also the electrical resistance of the (bulk) Pd electrolyte (R_e). Furthermore, the overall AAO template can be interpreted as a parallel resistor network, namely a parallel arrangement of a set of individual resistances that are associated with each pore [52]. These individual resistances include the resistance of the Al_2O_3 barrier at the bottom of the pore ($R\delta_B$), the resistance of the pore partial filled by metal (ρ_m) and the resistance of the remaining pore still filled with the Pd electrolyte ($\rho_e(t)$), as schematically shown in Fig. 2.8.

The porosity of the AAO is modulated through the template, decreasing from the dendritic pores tips towards the main AAO pores. This corresponds to a decrease in the inner surface area of the pores, where the Pd ion reduction occurs, during the fulfilling of the dendritic region. Thus, the associated increase in the electrical resistance leads to an increase in the measured V(t), as observed in the first minutes of electrodeposition (Fig 2.7) [55]. In principle, as the Pd filling achieves the main pores of the AAO, the V_{dep}(t) curve tend to stabilize due to the constant porosity of the AAO main region [55], phenomena which is only observed for the case of j_{dep} equal to 15 mA/cm^{2}or 25 mA/cm^2. In the rest of the curves, corresponding to higher j_{dep} (35 mA/cm^{2}or 45 mA/cm^2), the current does not reach a steady state value. This can be explained as result of a continuous depletion of the Pd ionic concentration inside the AAO pores [$\rho_e(t)$], which results in an increase of the electrical resistance and therefore, to the continuous increase of V_{dep}(t) [58]. Once the Pd NWs reach the top of the AAO template, as illustrated in the cross-sectional view SEM image of Fig. 2.9 b), the Pd start to be deposited as mushrooms caps. Due to the higher associated Pd surface and its uncontrolled increase, the deposition voltage V_{dep}(t) usually drops with noise. [52]. In this way, the applied voltage, V_{dep}(t), typically increase until the NWs reach the AAO top surface. In Fig.2.7 b) it is displayed the dependence of the measured applied voltage V(t) at the 1st deposition pulse (V_0), with the applied j_{dep}, revealing a linear ohmic behavior for the lower j_{dep} range (15-45 mA/cm^2) [57]. For the higher j_{dep} values, the linear behavior is no more observed because of the intrinsic resistance change (pore + electrolyte) due to the electrolyte concentration variation.

The growth rate of the nanowires results from a balance between of the Pd ion´s thermal diffusion, namely from the bulk electrolyte towards the bottom of the AAO pores, and the established pulse deposition current density (j_{dep}) imposed by the source [52,56].

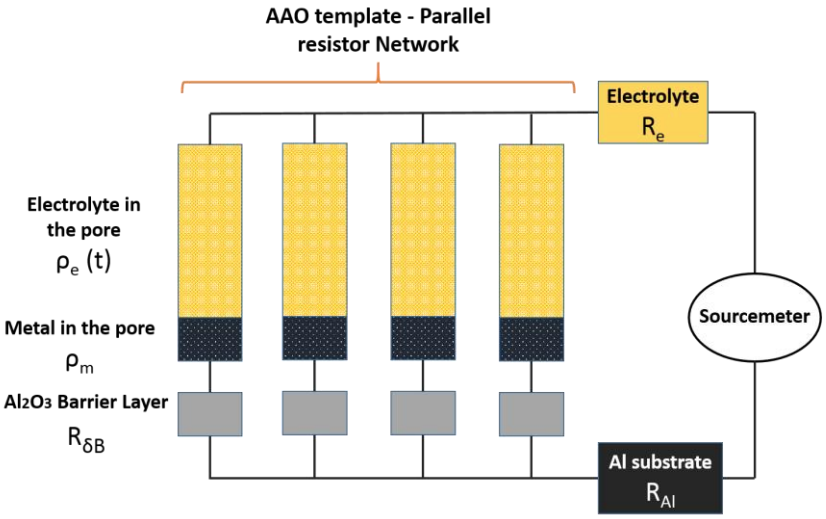

Figure 2.8: Illustration of the equivalent electrical circuit of the electrodeposition experimental setup and the parallel resistor network of the AAO template. The image was adapted from Ref. [52]

The established j_{dep} plays a major role in defining the growth quality of the NWs. From the micrographs obtained by SEM and displayed in Fig. 2.9 a), we observe for j_{dep} of 70 mA/cm^2 the best filling of the AAO template, where approximately 86% of the AAO pores are filled at the top of the template. However, if we compare the structural quality of the Pd NWs with the ones obtained from lower j_{dep}, for example 35 and 25 mA/cm^2 [Figs. 2.9 b) and 2.9 c)], it is clearly visible that the higher the applied $j_{dep,}$ the rougher the lateral surface of the Pd NW will be. This is evident by comparing the cross-sectional- and top-views micrographs. For the case of j_{dep} = 70 mA/cm^2, the Pd-filled AAO pores are not completely filled in its entire cross-section. In this later case, the excessive j_{dep} leads to a fast depletion of the Pd ions inside the pores, so that the growth of the Pd NWs becomes limited by the Pd ion diffusion [58]. Moreover, the resultant higher applied voltages, as seen in the measured deposition curves, $V_{dep}(t)$, result in a higher electric field intensity felt by the electrolyte ions. This is known to induce a preferential vertical growth of the NWs structure (parallel to the electric field lines) [56,57]. On the other hand and for the lower applied current density (j_{dep}), the associated lower growth rate, besides reducing the Pd ion concentration depletion in the AAO pores, allows for the random thermal diffusion of the Pd ions to completely fill the cross section of the AAO pores [57]. In this way the obtained NWs are much more compact, which results in considerably smoother lateral surfaces [Fig. 2.9 b) and 2.9 c)].

Furthermore, we also see, from the cross-section micrographs, a dispersion in the Pd NWs length. Fluctuations in the Al_2O_3 barrier thickness (δ_B) result in considerable deviations of the associated pore electrical resistance ($R\delta B$) [52]. The parallel arrangement of the AAO pores (Fig. 2.8), potentiates a different growth for neighboring pores, in accordance with the Kirchhoff circuit theory. For a parallel resistor network, through the branch with the lowest

electrical resistance will pass the higher intensity current. On the other hand, it is also observed dispersion of the NWs length on a macroscopic scale, which is evident if we compare, for example, the top view micrographs displayed in Fig. 2.9 b), taken at different locations of the sample. The presence of defects on the original Al foil, such as scratches, or a heterogeneous electrical field produced by a misplaced Pt grid, to mention a few, might lead to preferential Pd growth on some regions of the sample.

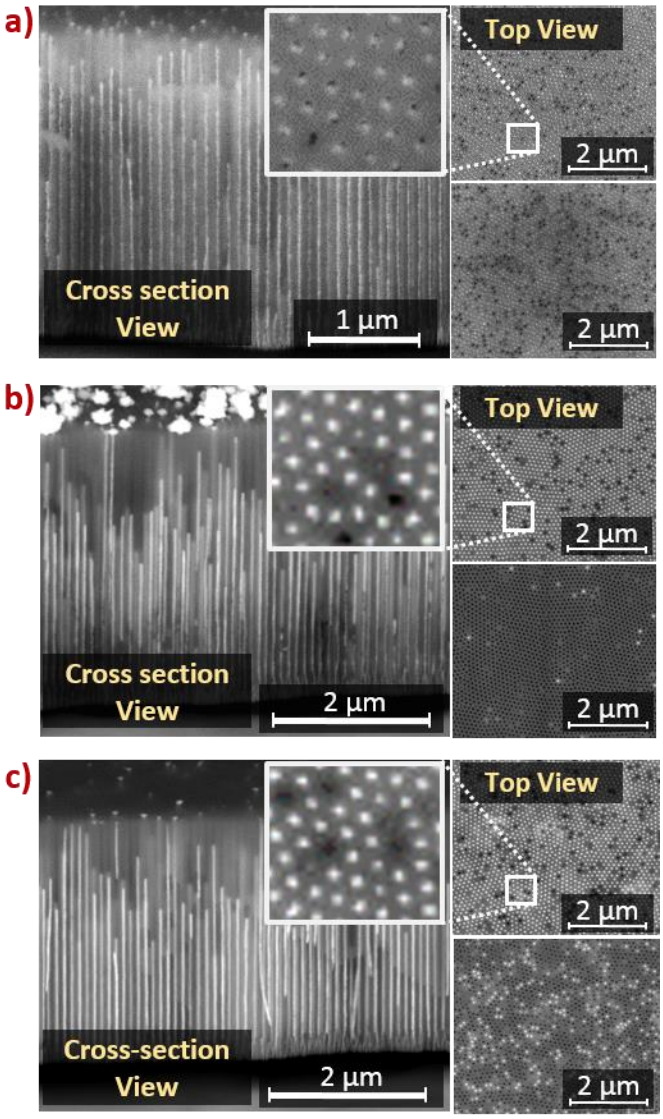

Figure 2.9: Scanning electron microscope (SEM) micrographs of the AAO templates and Pd Nanowires, obtained after the Pd PED. a) j_{dep} = 70 mA/cm^2 ;b) j_{dep} = 35 mA/cm^2 ;c) j_{dep} = 25 mA/cm^2. At the left side it is represented the cross section view of the Pd filled AAO template, while at the right side it is displayed the top view of the AAO surface at different locations of the sample. These were obtained after performing an ion beam milling of 500 nm.

During the electrodeposition process, it was observed gas bubbles emerging from the AAO template surface. It is known from the literature that the high cathodic potentials developed at

the Al_2O_3 barrier, lead to the evolution of hydrogen [52,54]. This can become the dominant process, when a depletion of the metal ionic concentration inside the AAO pores is high [56]. The formation of H_2(g) bubbles, that may be trapped in the AAO pores or at the AAO top surface, may inhibits the renovation of the electrolyte inside the corresponding pores, increasing also the NWs length dispersion [57]. These gas bubbles formation effects are stronger in the higher j_{dep} processes.

In Fig. 2.10 it is presented the typical measured energy dispersive spectroscopy (EDS) spectrum for the fabricated samples. The EDS reveal the presence of chemical elements such as the Al, O (from the AAO template and the Al substrate) and Pd (from the grown NWs). The presence of the C peak is attributed to the use of a conductive, carbon based, tape which is used to fix the analyzed samples to the SEM sample holders.

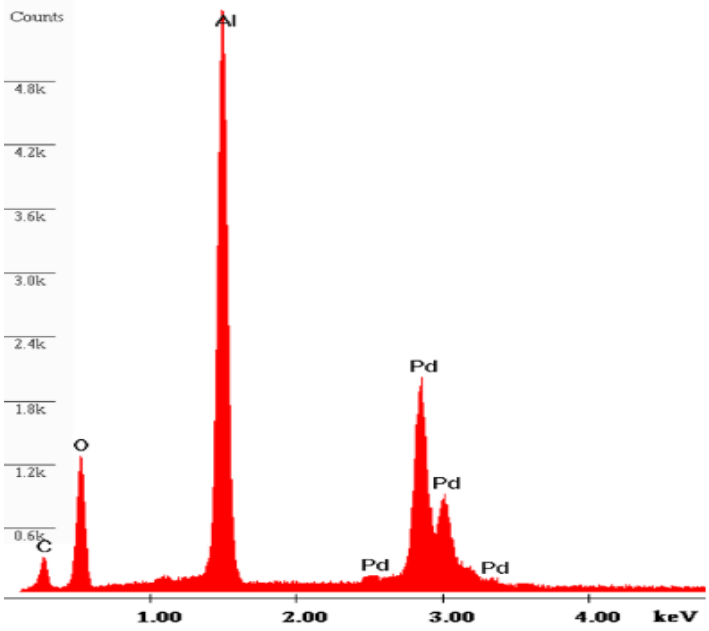

Figure 2.10: Typical EDS spectra obtained from the Pd electrodeposited AAO samples.

2.2.1.2. Chemical corrosion of the AAO template

It was noticed that in a few cases the SEM micrographs of the fabricated samples revealed a chemical corrosion of the AAO template, as illustrated in Fig. 2.11 a). Moreover, for long electrodepositions (higher than 80 min, using a j_{dep} of 35 mA/cm^2 and the aforementioned conditions), localized sections of the already Pd filled AAO templates started to be expelled from the Al substrate, originating a sudden drop in the deposition voltage. Ultimately a decrease in the electrical resistance indicates that the Al substrate had become exposed to the Pd electrolyte solution. Figure 2.11 c) exhibits the resulting set of cracks in the AAO template, through which Pd continued to be deposited. In Fig.2.11 d) it is displayed a cross-section

micrograph of the same sample in an undamaged region. Since the alumina is sensitive to acid solutions, as previously mentioned, it was thought that the acid solution of the Pd electrolyte (pH ≈ 2.5) was responsible for the destruction of the AAO template [52]. It was supposed that the dissolution of the AAO template weakened its structure, enabling latent residual mechanical stresses to expel sections of the AAO template.

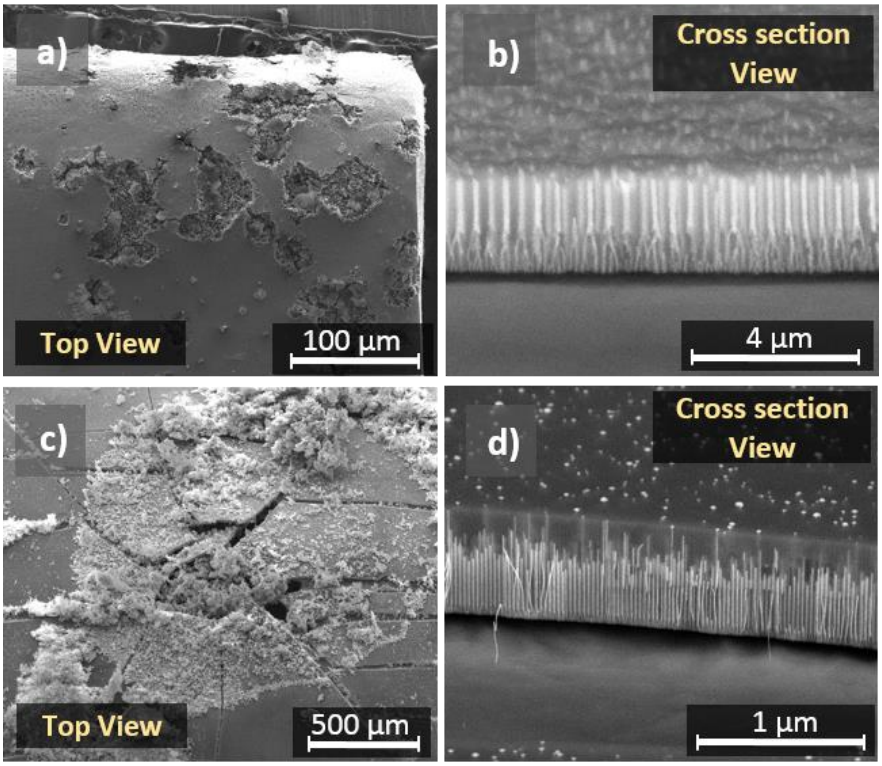

Figure 2.11: Scanning electron microscope (SEM) micrographs of the chemical corrosion of the AAO template. a) Top view and b) cross section view of an AAO sample obtained after PED of Pd, for which the Pd electrolyte temperature was raised to 40 ºC and a j_{dep} = 35 mA/cm^2 was used. c) Top view and d) cross section view of a sample obtained after a 80 min long PED, performed at room temperature and using a j_{dep} = 35 mA/cm^2.

In order to overcome this issue and to achieve a more controlled electrodeposition process, it was pursued to electrodeposit Pd with a neutral pH ionic solution. Based on Victor Vega's work, a second Pd-electrolyte, consisting in a 0.004 M $PdCl_2$ solution, was prepared with a neutral pH by the controlled addition of ammonia and hydrochloric acid [61]. The author reports the growth of Pd nanowires via a pulsed DC electrodeposition without mentioning any kind of degradation of the AAO template.

2.2.2. Palladium Chloride ionic solution

In order to prepare samples for optical measurements, we proceed with the electrodeposition of ~ 20 µm thick AAO templates, ensuring in this way their mechanical stability [52]. The electrodeposition of Pd was done in two different AAO templates, one with natural porosity

(≈11%) and the other with 31% of porosity. In the latter, the corresponding AAO pores were chemically widened in 0.5 M phosphoric acid aq. solution. For the Pd PED it was used a j_{dep} of 35 mA/cm^2 and a t_{dep} of 8 ms, a V_{dis} of 8 V with a duration (t_{dis}) of 2 ms and a rest pulse time duration of 0.7 s.

The measured deposition curves V_{dep}(t) (Fig. 2.12) show an increase during the first 15-16 min, after which the V_{dep}(t) suddenly drops. Also during the discharge pulse, the measured I_{dis}(t) increases abruptly, until it reaches a current limit imposed by the power supply for safety purposes. As shown in the inset photographs of the corresponding samples, we observe the formation of cracks in both AAO templates. In particular, on the sample at which it was performed the pore widening, a relative large portion of the AAO template became separated from the Al substrate. Moreover, it was also noticed in some cases that the sudden drop in the measured V_{dep}(t) was accompanied by a large bubble of gas emerging from the AAO template.

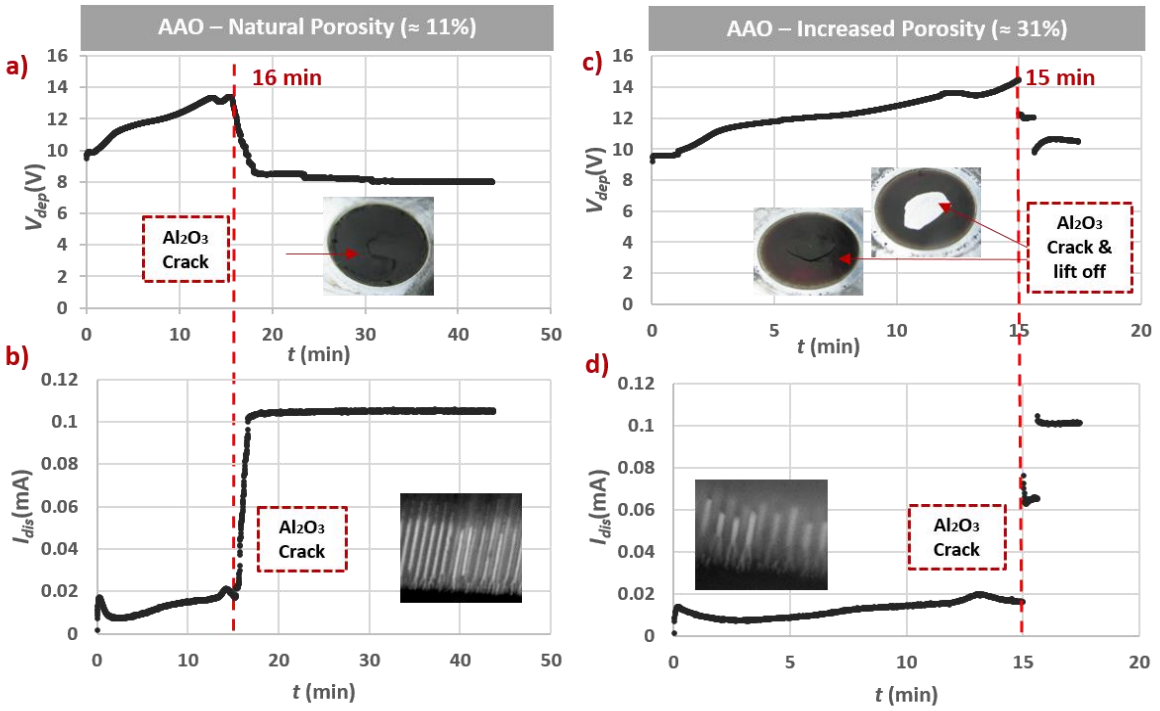

Figure 2.12 Representation of the deposition profiles of the measured V_{dep}(t) and I_{dis}(t), using a j_{dep} of 35 mA/cm^2 and a 0.004 M $PdCl_2$ aq. solution. Electrodeposition in an AAO template of 11% porosity a), b) and 31% porosity c), d). The inset photographs of the respective samples reveal the formation of cracks in the AAO template and also the exposure of the Al substrate.

Since the $PdCl_2$ electrolyte does not chemically attack the AAO template [61], the previous hypothesis that suggested a latent mechanical stress release through the partial dissolution of the AAO template was disproved. Furthermore, this phenomenon was observed earlier for this electrolyte, which suggests that the issue is related to a Pd-H co-deposition.

2.2.2.1. The Pd-H co-deposition

It is known from the literature that the fabrication of Pd films by DC electrodeposition is accompanied by the co-deposition of H, namely the adsorption of H atoms either through the reduction of H^+ (H_3O^+) ions present in the electrolyte or even from water hydrolysis [62,63]. Due to the large misfit between the lattice constants of pure Pd and the Pd-hydride in the β phase, this co-deposition usually leads to the formation of cracks and the flacking of the electrodeposited films during the latter H desorption [62,63]. In this way, the typical resulting Pd electrodeposited films appears as a black powdery film. In order to overcome this issue, authors have pursued to increase the efficiency of the Pd electrodeposition. This efficiency is defined as the percentage of electrons used only for the Pd ion reduction and not in the secondary undesired reactions, such as the hydrogen reduction. Several solutions can be adopted to improve the quality of the grown films, namely either by increasing the Pd ionic concentration or recurring to Pd neutral/alkaline solutions, or even by imposing agitation and increasing the electrolyte temperature. These factors allow to increase the relative concentration of Pd ions respect to H^+ (H_3O^+) ions near the electrode surface and enhancing the deposition efficiency [62]. When all these precautions are taken into account, it is possible to growth cohesive Pd films that present the typical Pd bulk metallic brilliance.

As mentioned before, the efficiency of the deposition pulse of PED can be limited by the hydrogen evolution, where the high cathodic potentials developed in the alumina barrier, established for the electrons to overcome the alumina barrier, induce the H_2 formation [52,56]. It is known that the H may be adsorbed in the growing structure, inducing defects, or even might be trapped as bubbles inside the AAO pores [58]. However, when dealing with the growth of Pd NWs by PED, this presents extra issues. The H atoms are able to diffuse easily through the growing structure because the deposited Pd corresponds to a permeable layer for the H [18]. Moreover Favier reports that the absorbed amount of hydrogen in electrodeposited Pd films can surpass the typical values, where it is reported that the Pd structures are found to absorb hydrogen more readily when they form the cathode of an electrolytic cell. Furthermore the author reports that the presence of the electrolyte at the Pd surface may inhibit the H desorption by poisoning of the Pd surface, which can lead to the exceeding increase in the atomic Pd:H atomic ratio [17]. Therefore, either due to a mechanical stress induced by the Pd expansion (due to HILE) or the accumulation of H_2(g) pockets in the interface between the AAO template and the Al substrate, the accumulated stress leads to the AAO deformation and its fracture, and in some cases to its partial separation from the Al substrate [inset of the Fig. 2.11 b)]. The

mechanism through which the migration of hydrogen through the alumina barrier would proceed and aggregate in the Al_2O_3/Al interface is not yet understood, but could be the explanation for the occasional observation of the simultaneous gas bubble. By comparing the two samples above, it seems that the templates with increased porosity are more prone to deformations/cracking under H induced stress, possibly due a weakening of the AAO structure. This is visible since the extent of the damages is clearly higher for the AAO template with the highest porosity (30%). Furthermore, the reason why this happens sooner in the 0.004 M $PdCl_2$ electrolyte than in the previous 0.0085M $Pd(NO_3)_2.2H_2O$ solution, possibly results from the lower Pd ionic concentration. The lower the Pd electrolyte concentration is the faster will be the drop in the Pd ion concentration near the AAO template, increasing in this way the deposition pulse inefficiency and the hydrogen co-deposition. From the inset SEM micrographs presented in Fig. 2.12, we can observe that the electrodeposition was interrupted during the Pd filling of the AAO main pores. As argued before, although it corresponds to a section of constant porosity, the continuous growth in the deposition curve V_{dep}(t) suggests a depletion of the Pd ionic concentration inside the AAO pores [55,58]. In order to obtain crack free Pd samples trough PED by using the previous mentioned conditions, the duration of the electrodeposition should be inferior to 15 minutes. This could be a problem when long NWs are desired but in our case, and due to the optical measurements that will be performed, NWs as long as 1 – 2 μm are sufficient for us.

2.2.2.2. The efficiency of the deposition pulse, the influence of j_{dep}, agitation and temperature

In order to reduce the suspected Pd-Hydrogen co-deposition, it is shown in Fig. 2.13 the effect of decreasing the deposition current density, j_{dep}. The Pd was electrodeposited via PED at room temperature and in 5 μm thick AAO templates, for an applied current density pulse, j_{dep}, of 35 mA/cm^2, 17.5 mA/^{cm2} and 8 mA/cm^2, respectively. A duration of 8 ms for the deposition pulse, a discharge pulse of 8 V and 2 ms duration, as well a 0.7 s rest pulse were commonly used as the remaining parameters.

The V_{dep}(t) deposition curves show that reducing j_{dep} to 17.5 mA/cm^2 allows to extend the electrodeposition time (before the hydrogen embrittlement take place) to 42 min, more than the double of the time we could apply when using a j_{dep} of 35 mA/cm^2. Moreover, it is obtained a growth rate (G.r.) of 3.3 μm/h for j_{dep} = 17.5 mA/cm^2, which is 34% higher than what we would expect if we considered the growth rate of 4.9 μm/h, obtained for j_{dep} = 35 mA/cm^2. It is assumed a linear relation between the G.r. and the applied j_{dep}. However and as it is plotted in Fig. 2.14,

the linear relation is incorrect. We observe from the tendency line that by reducing the applied current density, j_{dep}, we are able to increase the efficiency of the deposition pulse.

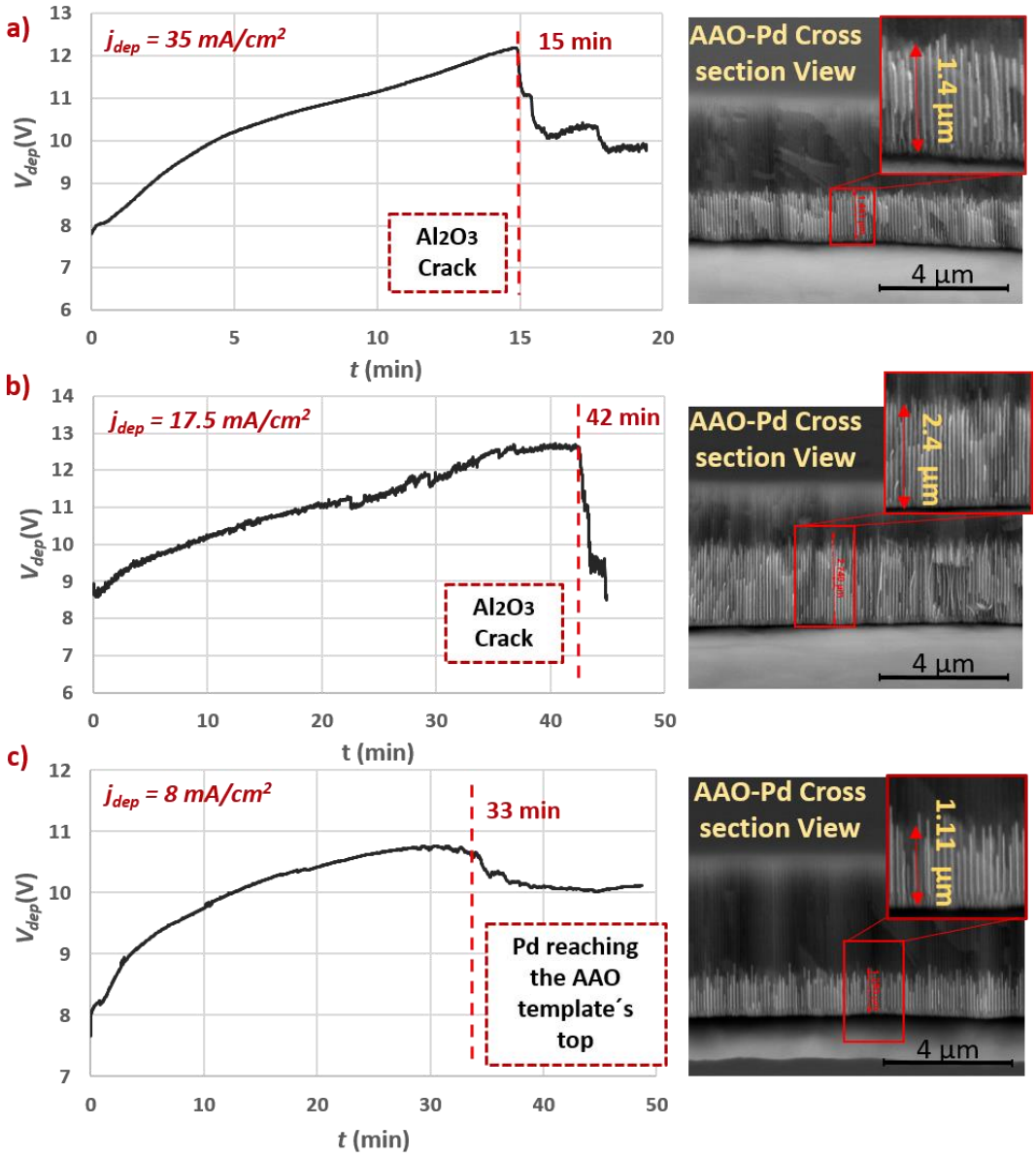

Figure 2.13: Deposition profiles of the measured V_{dep}(t) for a decreasing j_{dep} of a) 35 mA/cm^2, b) 17.5 mA/cm^2 and c) 8 mA/cm^2. At the left side of each plot, it is displayed a cross section SEM micrograph of the respective sample.

Table 2.2- NWs growth rate and length dispersion as a function of the applied j_{dep}.

j_{dep} (mA/cm2)	Dep. time (min)	< $L_{template}$ > (µm)	< L_{NW} > (µm)	L_{NW} Rel. Dispersion (%)	Growth rate (µm/h)
35	17 +/-2	4.30	1.4	5.7	4.9 +/- 0.9
17.5	44 +/-2	4.30	2.4	5.8	3.3 +/- 0.3
8	41 +/-8	4.64	1.11	16	1.6 +/- 0.6

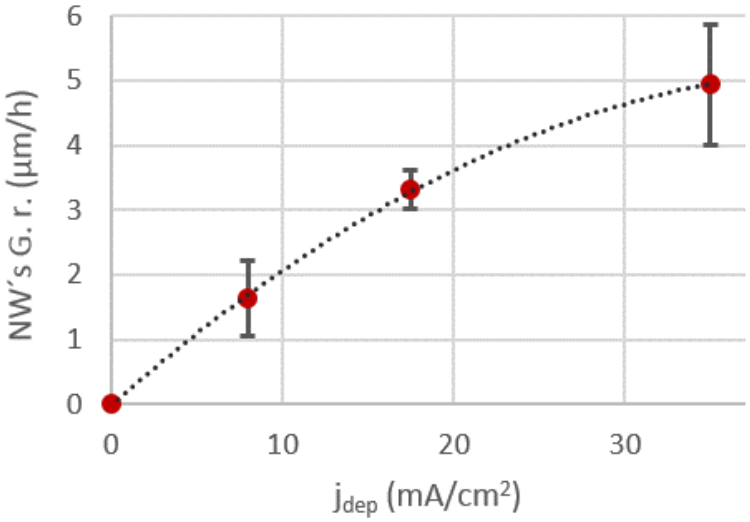

Figure 2.14: NWs growth rate dependence on the applied pulse current density, j_{dep}.

In the case of a j_{dep} = 8 mA/cm^2, instead of having an abrupt decrease in the deposition curve V_{dep}(t), it is observed instead a slower drop in the measured voltage after 33 min of electrodeposition, consistent with Pd NWs reaching the top of the AAO template. The pulsed electrodeposition was interrupted after 48 min, since it was confirmed that Pd had reach the top of the AAO, but only at the border of the sample, which was growing as a white Pd suspended filament. A defect in the sample could be a possible explanation for the enhanced localized Pd growth. Therefore, considering the respective micrographs images obtained by SEM at the center of the sample and even that the effective density current flowing in this region is lower than the initial one, we can estimate a lower limit for the growth rate of 1.6 µm/h, indicating once more an increase in the efficiency of the deposition pulse. When comparing the relative dispersion in NWs length with the other two samples, we observe an increase from 5.8 % to 16 % (see table 2.1). As the applied j_{dep} decrease, the NWs growth rate (rate of the Pd ions reduction) become limited by the proper j_{dep}, being more sensitive to fluctuations in the alumina barrier thickness and to the intrinsic parallel resistor arrangement of the AAO template, leading to a higher dispersion in the NWs length [52,57]. In contrary, when using higher j_{dep}, the growth becomes limited by the diffusion of the Pd ions to the bottom of the pores. This means that during a deposition pulse and once the current flows primarily through the pores with a thinner Al_2O_3 barrier (δ_B), the reduction of the Pd ions to Pd (s) inside those pores, leads to a drop in the local Pd ionic concentration. This momentarily increases the resistivity of theses pores [ρ_e(t); Fig. 2.8], so that the remaining electron current flows through the rest of the pores, the ones which have a thicker Al_2O_3 barrier. In this way the fluctuations of the Al_2O_3 barrier are compensated by the instantaneous increase in the pore-electrolyte resistivity ρ_e(t) [52]. As a result, an excessive decrease in j_{dep}, although allowing to increase the Pd deposition efficiency,

comes with the cost of obtaining a high NWs length dispersion due to the inhomogeneity's present in the Al_2O_3 barrier.

Using the same PED parameters and in order to increase the replenishment of the Pd ion concentration inside the AAO pores, it was tested the effect of both using agitation (150 rpm) and increasing the electrolyte temperature (38-40 ºC). The measured curves (Fig. 2.15) show no sign of AAO cracking, possibly indicating an increase in the efficiency of the deposition pulse. Moreover, the time needed for the NWs to fulfill the membrane is two times larger for the j_{dep} of 17.5 mA/cm^2 than in the j_{dep} of 35 mA/cm^2, indicating that the deposition is limited by the applied current. From the SEM micrographs, we have noticed a heterogeneous growth in the sample, namely a tendency of increasing NWs length from the center to the border of the sample. As shown in Fig. 2.15 c), the Pd has reached the top of the template near the border of the AAO template. This was already discussed in Ref. [57], where it is suggested that the stirring of the electrolyte induces vortices in the electrolyte above the samples, due to the experimental setup, creating an ionic concentration gradient.

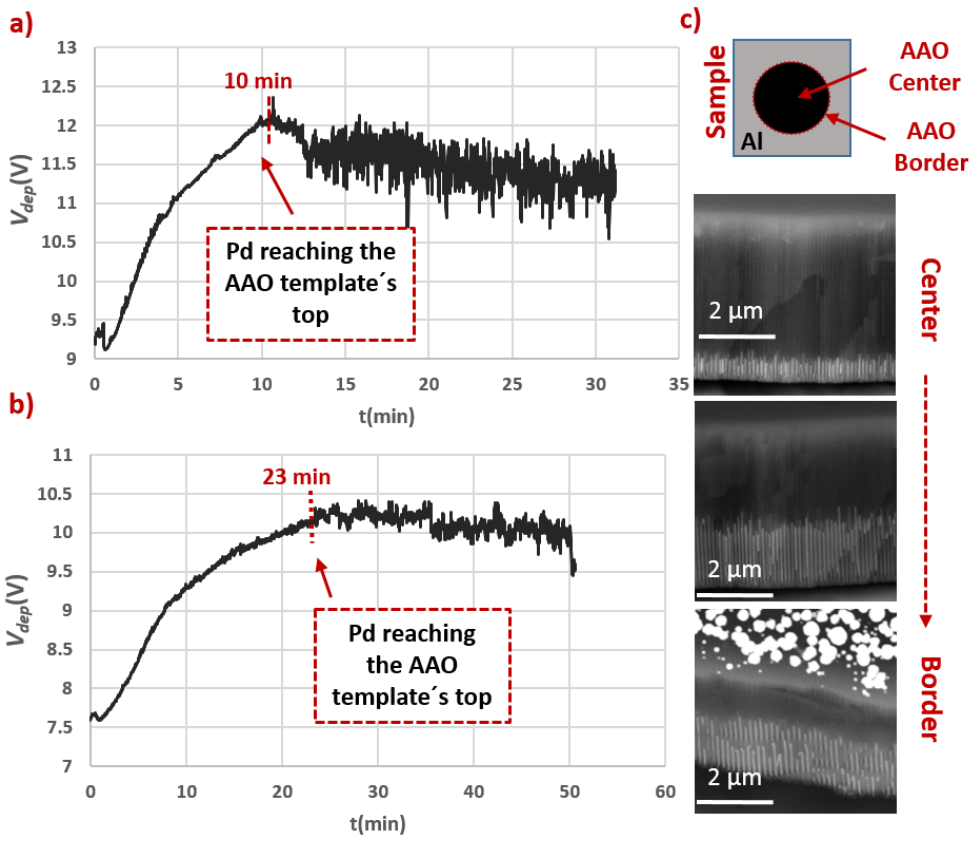

Figure 2.15: Deposition profiles of the measured V_{dep}(t) obtained when employing stirring (150 rpm) and increasing the $PdCl_2$ electrolyte temperature to 38-40 ºC. It was used a j_{dep} of 35 mA/cm^2 and 17.5 mA/cm^2, displayed respectively in a) and b). At the left side c) it is presented the SEM micrographs with the macroscopic NWs length dispersion from the center towards the border of the sample.

2.2.2.3. Monitoring the quality of the deposition and length of NWs through a Fabry-Pérot light interference

Working with the $PdCl_2$ electrolyte besides not chemically attacking the AAO template also has the advantage of being a colorless and transparent solution. Hence it enabled us to detect in the first minutes of the PED that the Pd deposition in the AAO samples was accompanied by color changes. The AAO template grown in the standard anodization conditions, namely at 40 V in oxalic acid, appears as a transparent template. However, once the AAO pores begin to be filled with Pd, the samples begin to acquire color. This is explained by the Fabry-Pérot (F.P.) interference phenomena, as illustrated in Fig. 2.16.

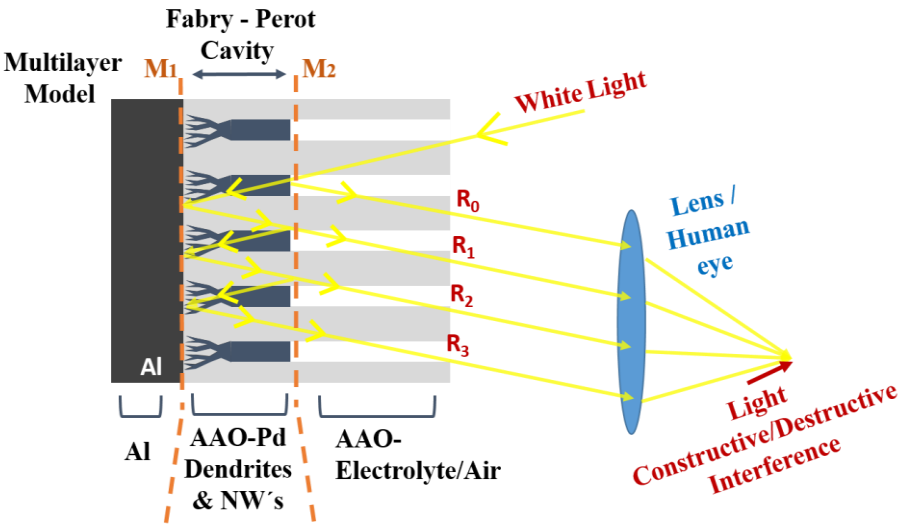

Figure 2.16: Schematic representation of the Fabry-Pérot light interference associated with the Fabry-Pérot cavity formed by the AAO template filled with Pd dendrites and NWs.

As the NWs grow they form a F.P. cavity, in which its reflecting surfaces (M_1 and M_2) are formed by the Al surface at the bottom of the pores and the interface between the Pd-filled AAO template and the unfilled AAO template at the top of the pores, as illustrated in Fig. 2.16. Once the light travels through the Pd filled-AAO medium, the successive light reflection between the two interfaces give rise to the F.P. interference effects. The resulting color of the sample correspond to the portion of the reflected visible spectrum for which the F.P. interference is constructive, namely when the multiple reflected light rays are in phase with each other [65]. The phase difference δ^{λ} between the successive reflected beam, e.g. R_0 and R_1 represented in the diagram, is dependent on the wavelength of the incident light (λ), the corresponding refractive index of the AAO-Pd medium (n^{λ}_{AAO-Pd}), the angle of propagation (θ), but more importantly on the thickness of the Pd-filled AAO template, which is equal to the total length

of the growing Pd dendrites and NWs. The corresponding phase difference can be calculated through the following expression [65]:

$$\delta^{\lambda} = 2\, n^{\lambda}_{AAO-Pd} L_{NW}\, cos(\theta) \left(\frac{2\pi}{\lambda}\right) \quad (2.\ 1)$$

Therefore as the AAO dendritic and main pores are filled with Pd, the length of the F.P. cavity increases and the resulting constructive interference peaks move across the electromagnetic spectrum, changing the color of the sample (Fig. 2.17). In this way, we are able to monitor by optical means not only the length of the NWs (Fig. 2.18), but also the uniformity of the electrodeposition across the sample (Fig. 2.19).

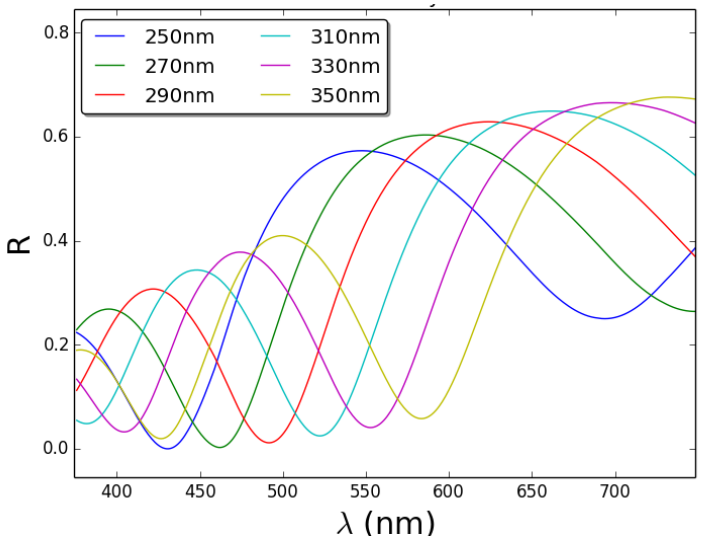

Figure 2.17: Spectral reflectance curves simulated for samples with increasing length of Pd NWs. The calculations are based on the Maxwell-Garnett homogenization model [66] and on the Transfer Matrix Method [67] (see appendix A for further info). The reflectance spectra correspond to normal incidence and it was assumed a constant porosity of 11% for the AAO template.

It was performed three electrodepositions with the following parameters: j_{dep} = 35 mA/cm^2 and 8 ms duration, V_{dis} = 8 V and 2 ms duration, and also 0.7 s rest pulse time duration. The corresponding obtained electrodeposition curves V_{dep}(t) (Fig. 2.18) show no sign of AAO deformation, as the electrodepositions were interrupted before hydrogen embrittlement took place (< 15 min). The chosen times are displayed in the inset table of Fig. 2.18 a). In Fig. 2.18 b) it is shown the respective SEM micrographs of the obtained samples, showing no signs of hydrogen induced defects, and in Fig. 2.18 c) it is shown the corresponding cross-section micrographs. Thanks to the F.P. interference, we are able to identify by the color changes of the sample different stages of the Pd NWs growth, e.g. the instant where the AAO dendrites become completely Pd-filled, the green color exhibited by sample D2. An increase of the order of 70 nm in the Pd NWs length correspond to a significant change in the color of the sample

from green (sample D_2) to purple (sample D_1). For sample D3, where only the dendritic pore tips were filled by Pd, a duller grey color is seen. For samples with Pd nanostructruture´s length higher than 500 nm, the color grows darker until it become black due to the increasing light absorption effects. In Fig. 2.18 b) the darker circular shape present in the middle of the samples, correspond to a region of the AAO template in which the Al substrate was chemically removed for optical measurements. Once removed the Al, the provided high reflectivity of M_1 (Fig. 2.16) disappears, resulting in an intensity decay of the Fabry-Pérot interference and sample´s color.

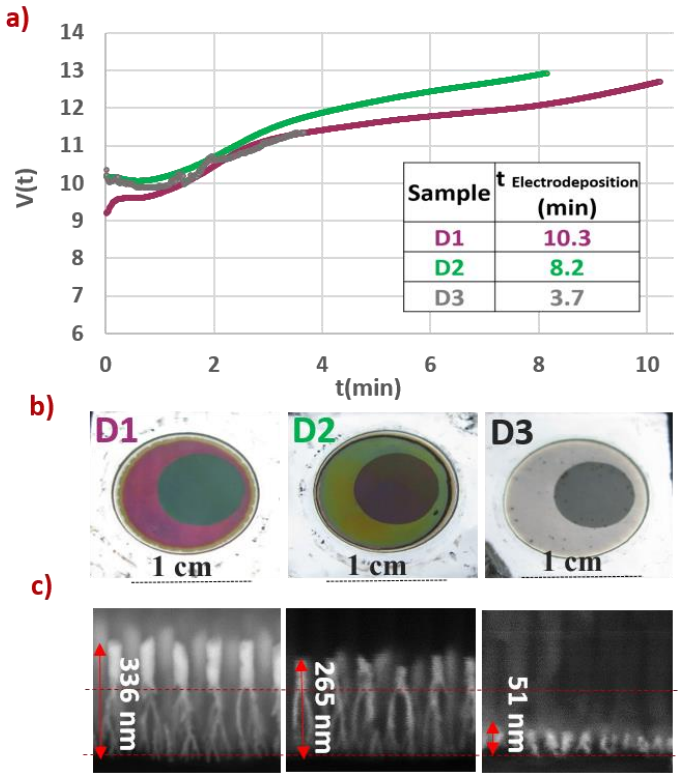

Figure 2.18: a) Deposition curves V_{dep}(t) and the respective electrodeposition time duration ($t_{Electrodepostion}$). b) Photographs of the corresponding samples, taken after a partial removal of the Al substrate at the center of the samples. c) SEM cross-section micrographs of the corresponding samples.

Additionally, the F.P. interference allows us to monitor in real time the quality of the grown samples, namely to infer if the deposition proceeds uniformly in the entire AAO template (Fig. 2.19). For instance, at the border of the sample exhibited in Fig. 2.19 a) we can see a gradient of colors. Thus, we are able to infer in that region a decay in the NWs length towards the border. In this case, the NWs growth was limited by the Pd ions diffusion since it was used a high j_{dep} of 35 mA/cm^2. The presence of the rubber O-ring seal (as shown in the experimental setup) close to the top of the AAO template seems to delay the diffusion of the ions into that region, resulting in slower Pd growth. On the other hand, Fig. 2.19 b) corresponds to a sample grown at the same electrodeposition conditions as previous sample. Either due to an inhomogeneous distribution of the electric field, caused by the misplaced Pt electrode grid, or sample defects,

it is shown an example of a sample with a high dispersion in the NWs length at a macroscopic scale. In Fig. 2.19 c) it is represented the initial deformation of the AAO template from the Al substrate due to hydrogen co-deposition. After an excessive electrodeposition duration (18 min for a j_{dep} of 35 mA/cm^2), in the regions where the Al_2O_3 is deformed and became separated from the Al substrate, the disruption of the F.P. cavity resulted in the loss of the previously obtained green color.

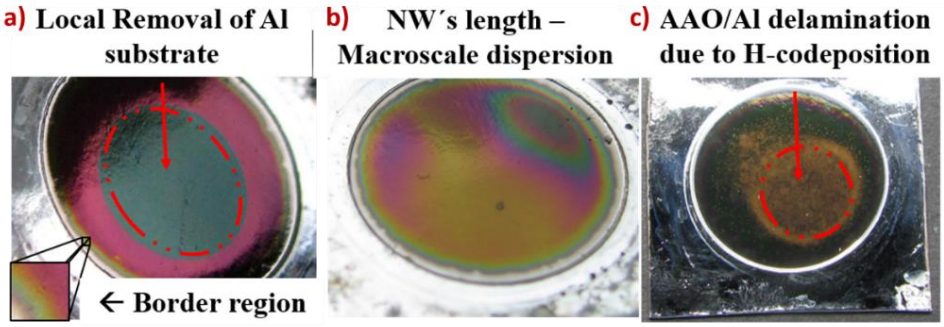

Figure 2.19: Monitoring NWs length dispersion and the quality control through the F.P interference. a) Border deposition effects, local removal of the Al substrate at the center of the sample; b) Example of a sample exhibiting a high NWs length dispersion; b) Disruption of the Fabry-Pérot cavity due to the H-induced AAO and Al delamination.

Chapter 3

Hydrogen optical sensor based on Pd dendritic nanostructures

In this chapter we present a new type of hydrogen optical sensor based on the fabrication of Pd dendritic nanostructures. Herein we describe the preparation of Pd samples for their functionalization as H_2(g) optical sensors. The sensor response to the presence of H_2(g) were characterized, at room temperature, by optical transmission measurements. We take into account the effects of the Pd-hydride phase transition and its size dependency to explain the kinetics of the hydrogen absorption and desorption in the studied samples. We demonstrate how this sensor can be employed to monitor hydrogen gas concentration either by measuring the rate of signal decay during the Pd hydrogen absorption (transient regime) or by measuring the total variation in signal once the Pd hydride system achieves the equilibrium state (stationary regime). The fabrication and functionalization of the Pd dendritic nanostructures were performed in the laboratories of IFIMUP-IN, while the optical characterization of the H_2(g) sensors was performed in the laboratories of INESC-CAP.

3.1 Fabrication of the Pd samples and their functionalization as H_2(g) sensors

At this stage of the experimental work we were motivated to study the use of Pd dendritic nanostructures as a mean to develop optical Pd-based H_2(g) sensors through an industrially friendly fabrication method.

In order to obtain a homogenous growth of the Pd nanostructures across the samples and reduce nanostructures length dispersion, the PED´s were performed in a 0.004 M $PdCl_2$ aqueous solution with the following conditions: j_{dep} = 35 mA/cm^2 and 8 ms duration, V_{dis} = 8 V and 2 ms duration, and a rest pulse of 0.7 s. It was used ~ 20 µm thick AAO templates to ensure mechanical stability to the samples. Moreover, two electrodepositions of 10 min and 4 min at 25 ºC were made to study the dependence of the sensors response on the Pd nanostructures'

size. Therefore, we have prepared samples consisting of either Pd dendrites + NWs (sample S1) or only Pd dendrites (samples S2 and S2*), respectively (see table 3.1 for further details).

In Fig. 3.1 it is displayed the SEM micrographs of the fabricated samples. Figure 3.1 a) depicts in detail the AAO template filled with Pd dendrites and NWs (sample S1), obtained after 10 min of electrodeposition. It is observed how the Pd nanowires, with an average length of 100 nm and a diameter of 70 nm, divide into several Y shape ramifications, the dendrites. Figure 3.1 b) depicts the Pd Y-nanostructures, obtained after the Pd (partial) filling of the AAO dendritic pores.

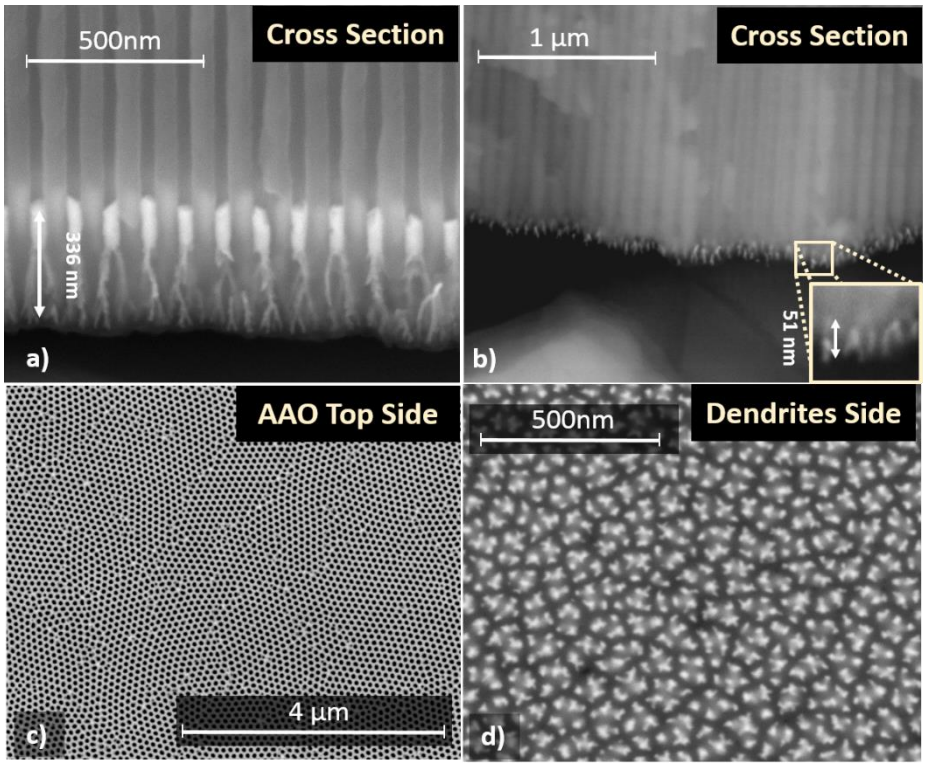

Figure 3.1: Scanning Electron Microscope (SEM) micrographs of the sample S1 and S2 - a) and b) Cross-sectional view revealing the Pd nanostructures of sample S1 (dendrites + NWs) and S2 (dendrites), respectively; c) and d) Top view depicting the top of the AAO template and the exposed dendrites tips (sample S1), respectively.

The Al foil substrates at the center of the samples were chemically removed (Fig. 3.2) to allow the optical characterization of the samples by transmission measurements. Afterwards the 10 nm alumina barrier, which remained between the bottom of the Pd nanostructures and the atmosphere, was chemically etched in order to expose the tips of the Pd dendrites. The alumina etching was performed in a 0.5 M H_3PO_4 aqueous solution for 15/30 min at 30ºC, according to an alumina dissolution rate of 1 nm/min, see table 3.1 for further details. Figure 3.1 d) illustrates the exposed tips of the Pd dendrites that enable a fastest capture and hydrogen absorption. Despite the unfilled pores of the AAO template are in direct exchange with the atmosphere, they present huge impedance to the H_2 molecular flow due to its high aspect ratio of 20000 nm

x 70 nm. The effects of the alumina barrier etching on the response time of the samples to H_2(g) is displayed above in sect. 3.2.

Table 3.1 - Fabrications parameters of the studied samples.

Samples	Electrodeposition time (min)	Pd nanostructure type	Alumina barrier etching time (min)
S1	10	Dendrites + NWs	15
S2	4	Dendrites	15
S2*	4	Dendrites	30

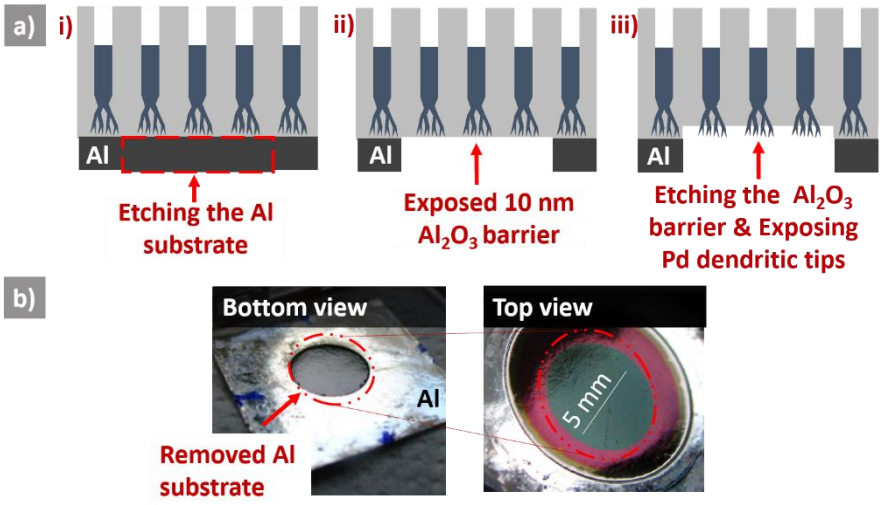

Figure 3.2: a) Representative illustration of the functionalization of the Pd samples for H_2(g) optical sensing (illustrations not to scale); b) Photograph image of the functionalized S1 sample.

3.2 Characterization of the sensor's optical Response - experimental Protocol

The optical transmission response of the samples were studied during H_2(g) exposures in the range of 1% to 12% concentration (% v/v) in air. In order to characterize the time response of the sensors, the transmitted light spectrum through the samples was measured during the Pd-hydrogenation and de-hydrogenation cycles. The samples were mounted inside a stainless steel gas chamber with two optical fiber feedthroughs, one gas inlets and one gas outlet as seen in Fig. 3.3. The two optical fibers (Thorlabs multimode SMA-SMA optical fibers 105 µm diameter, Numeric Aperture 0.22) were connected to collimators (Ocean Optics 74-VIS) mounted inside the chamber, each serving as light source and collector, respectively. In this configuration the light is injected into the samples in a direction parallel to the NWs. It was used a tungsten-halogen lamp (Avantes AvaLight-Hal) as an unpolarized light source and a CCD spectrometer (Ocean Optics USB-4000-VIS-NIR) to record the transmitted spectra. During the hydrogenation cycles the samples were exposed to high purity mixtures of H_2 (4%

and 1% in volume, nominal) in N_2 at room temperature. In order to obtain the sensor calibration curves, the variation of the H_2(g) concentration was done by changing its partial pressure inside the chamber. Once the Pd-hydride system achieved the equilibrium, the H_2 mixtures inside the chamber were extracted through a vacuum pump and replaced by a pure N_2 atmosphere, to study the dehydrogenation kinetics of the Pd nanostructures.

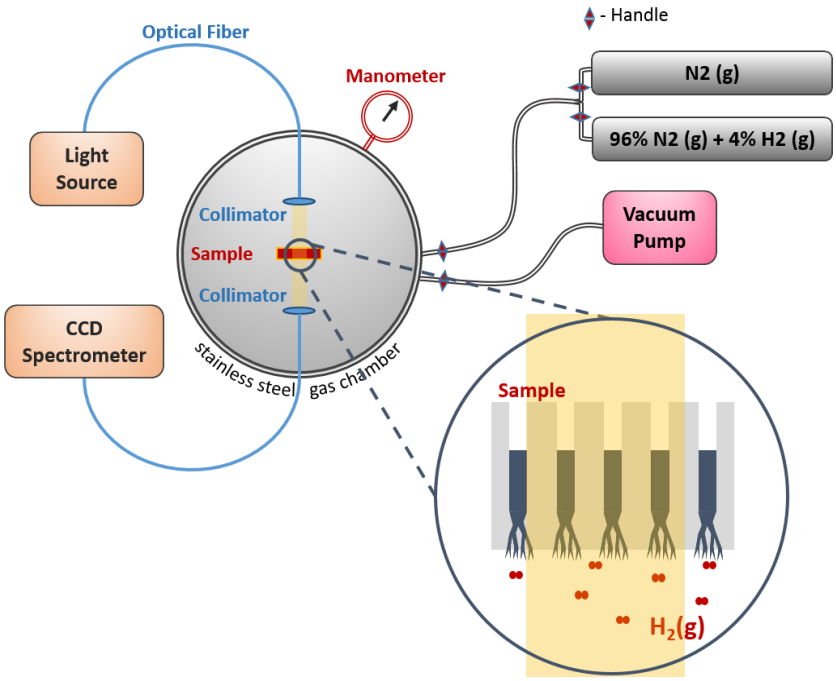

Figure 3.3: Experimental optical setup.

3.3 Optical transmission spectra of the samples to H_2(g)

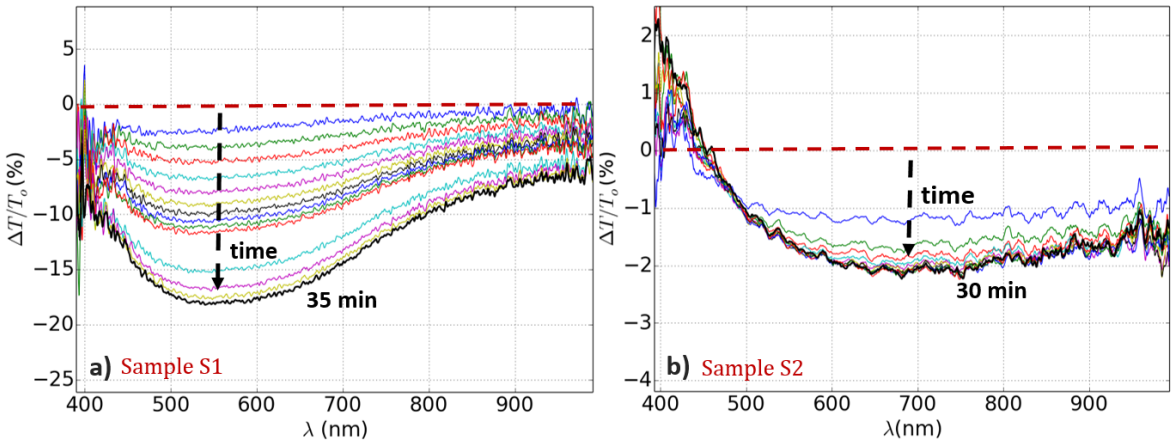

Figure 3.4: Spectral optical response of the sample S1 (a) and S2 (b) when exposed a H_2(g) partial pressure of 0.049 atm**.**

In Fig. 3.4 it is shown the spectral optical response of the sample S1 and S2, when exposed to a H_2(g) partial pressure (p.p.) of 0.049 atm. The sensitivity ($\Delta T/T_0$) was calculated as the relative variation in transmitted light intensity with reference to T_0, where T_0 corresponds to the

measured transmitted light intensity in a pure N_2 atmosphere, before exposing the Pd samples to H_2(g).

It can be observed that sample S1 (Pd dendrites + NWs) exhibits a pronounced decrease in its transmission, reaching a maximum decay ($\Delta T/T_0$) of 17.5 % at a wavelength of 550 nm and after 35 min exposure to H_2(g). On the other hand, sample S2 shows a maximum decay of ~2%, red shifted in the visible spectrum to ~700 nm. Moreover and unlike sample S1, the transmitted light intensity for sample S2 shows a negligible variation near the wavelength of 470 nm. Additionally, the $\Delta T/T_0$ response for light wavelengths below the 470 nm increases with the exposure time of H_2(g).

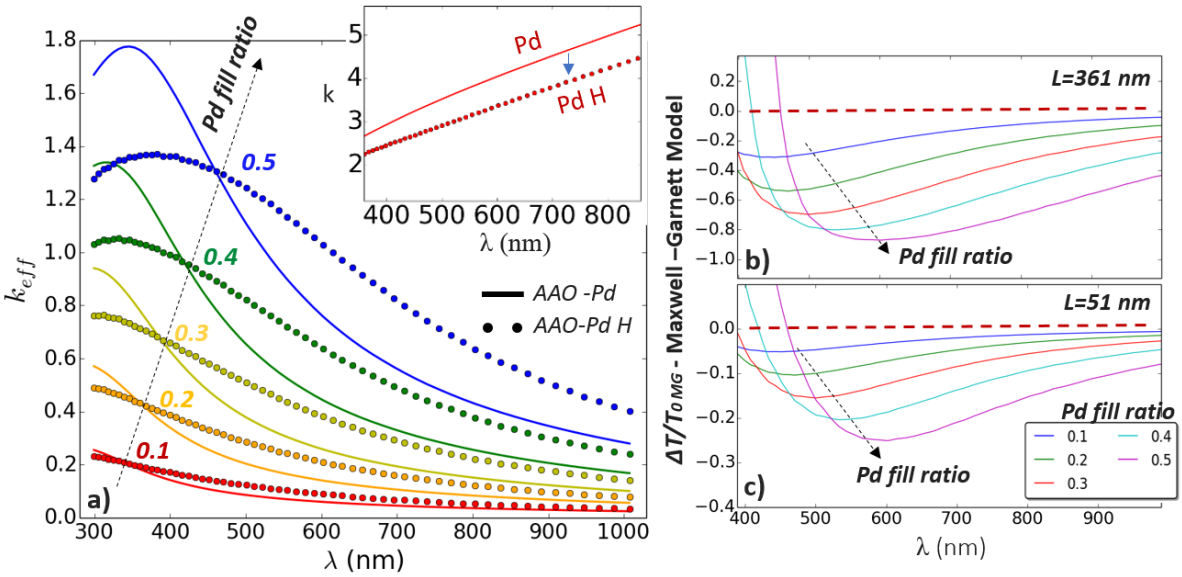

Figure 3.5: a) Comparison between the effective extinction coefficient (*keff*), obtained via the Maxwell-Garnett Model, for the AAO-Pd and AAO-Pd hydride composites as a function of the Pd fill ratio. In the inset graph it is plotted the extinction coefficient *k* of Pd and Pd hydride taken from Ref. [32]; b) and c) Calculated $\Delta T/T_{0_{MG}}$ as a function of Pd fill ratio for a AAO-Pd thickness (L) of 361 nm and 51 nm, respectively.

As it was previously noticed by Aurelio et all in a previous work resulting from a collaboration between INESC-CAP and IFIMUP, the optical response of this type of sensors is dictated not only by the Pd inclusions but also by the light interactions with its surrounding medium, the AAO template [68]. As displayed at the inset of Fig. 3.5 a), although the Pd extinction coefficient in the visible range decrease during the Pd hydrogenation [32], a refractive index matching condition between the Pd-structures and the AAO template results in an increase of light absorption [68]. This behavior is predicted by the homogenization model of Maxwell-Garnett (M.G.) as represented in Fig. 3.5 a), where it is compared the effective extinction coefficient (k_{eff}) between the AAO-Pd and the AAO-Pd:hydride composites as a function of the

Pd fill-ratio (defined as the geometrical ratio of Pd within the composite AAO-Pd). The resulting relative variation in transmitted light intensity $\left(\Delta T/T_{0_{MG}}\right)$ predicted by the model, as displayed in Fig. 3.5 b) and 3.5 c), exhibits a similar profile of the experimental measured $\Delta T/T_0$ spectra. Moreover, the M.G. model shows that as the Pd fill-ratio increases, the response of the composite AAO-Pd to H_2(g) gradually tends toward the Pd natural's response. This results in the gradual increment of the transmitted light in the blue region of the visible spectrum and also in a redshift correspondent to the wavelength of maximum $\Delta T/T_0$ decay. This tendency is experimentally verified (Fig. 3.4), if we take into account that sample S2, uniquely composed by the Pd-filled dendrites, has a higher effective Pd fill-ratio when compared to sample S1.[1] In addition, the calculations presented for $\Delta T/T_{0_{MG}}$ correspondent to the AAO-Pd of 51 nm and 361 nm thick (L), reveal that the higher length of the Pd nanostructures allow to increase the sensor´s sensitivity to H_2(g).

3.4 Optical time response of the samples

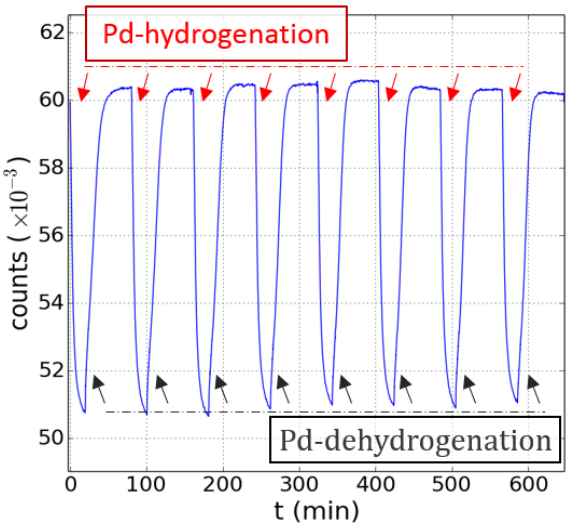

Figure 3.6 Transmission response of sample S1 to H_2(g) partial pressure of 0.049 atm at room temperature and at a selected wavelength of 633 nm. The sample S1 was submitted to 8 continuous hydrogenation and dehydrogenation cycles

In Fig. 3.6 it is represented the time response of the sample S1, at a selected wavelength of 633 nm, when exposed consecutively to a H_2(g) partial pressure (p.p.) of 0.049 atm (hydrogenation cycle) and a pure N_2(g) atmosphere (dehydrogenation cycle). Once more during the H exposure cycles it is seen the decrease in the respective transmitted light intensity, while during the H-

[1] As mentioned earlier the AAO dendritic pores are associated with a higher porosity than AAO main pores [55].

desorption's cycle's the transmittance return close to its previous value, demonstrating the reversibility of the Pd-hydrogenation at room temperature and also the feasibility of the sample to be used for H_2(g) sensing.

In Fig. 3.7 it is represented the enhancement in the optical response time of the samples via the chemical etching of the alumina barrier and the subsequent exposure of the Pd dendrites. It is clearly visible that the high aspect ratio of 20000 nm x 70 nm of the unfilled AAO pores present a huge impedance to the H_2 molecular flow, this is evident by comparing the rate of variation of the sample transmittance before and after the alumina barrier chemical etching.

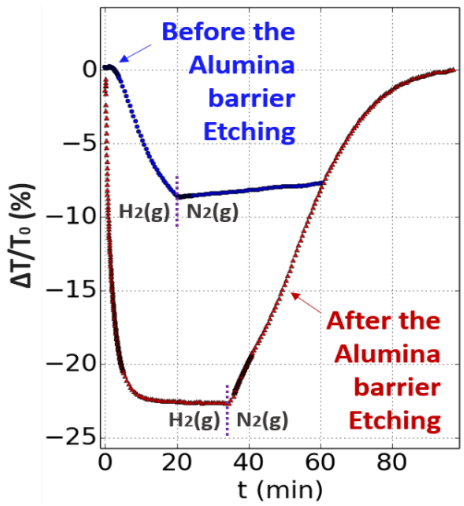

Figure 3.7 Comparison of the optical time response of sample S1 to a H_2(g) partial pressure of 0.12 atm at room temperature and at a selected wavelength of 633 nm, before and after the etching of the alumina barrier. The sample S1 was submitted to an H_2(g) exposure of 20 and 35 min, respectively, after which the sample was submitted to a pure N_2 atmosphere.

3.4.1 Study of the hydrogenation of the Pd samples

The optical response of samples S1 and S2 were studied for distinct H_2 concentration exposures, at the selected wavelength of 633 nm, as it is illustrated in Fig. 3.8. The increase in H_2 p.p. leads to the increase in the Pd structure´s H content that results in a continuous change in the Pd refractive index [38]. This results in the gradual increase of the effective extinction coefficient of the AAO-Pd hydride composite (at the 633 nm wavelength), leading to a gradual decay of the samples transmittance.

A Python program was developed and used to perform the analysis of the obtained data. The solid lines presented in Fig. 3.8 correspond to fitted curves from the experimental data, obtained according to the following equation:

$$f(t) = A\left(1 - \exp\left(\frac{\ln(0.05)t}{\tau_{eq}}\right)\right). \quad (3.1)$$

The proportionality constant A corresponds to the relative variation in the transmitted light intensity, measured once the system achieves the equilibrium state ($\Delta T_{eq}/T_0$). The characteristic time, τ_{eq}, corresponds to the time that the Pd-hydride system takes to achieve the same equilibrium state (more specifically 95% of the total variation in $\Delta T_{eq}/T_0$). Both the obtained $\Delta T_{eq}/T_0$ and τ_{eq} are plotted in Fig. 3.9 as a function of the H_2(g) p.p.

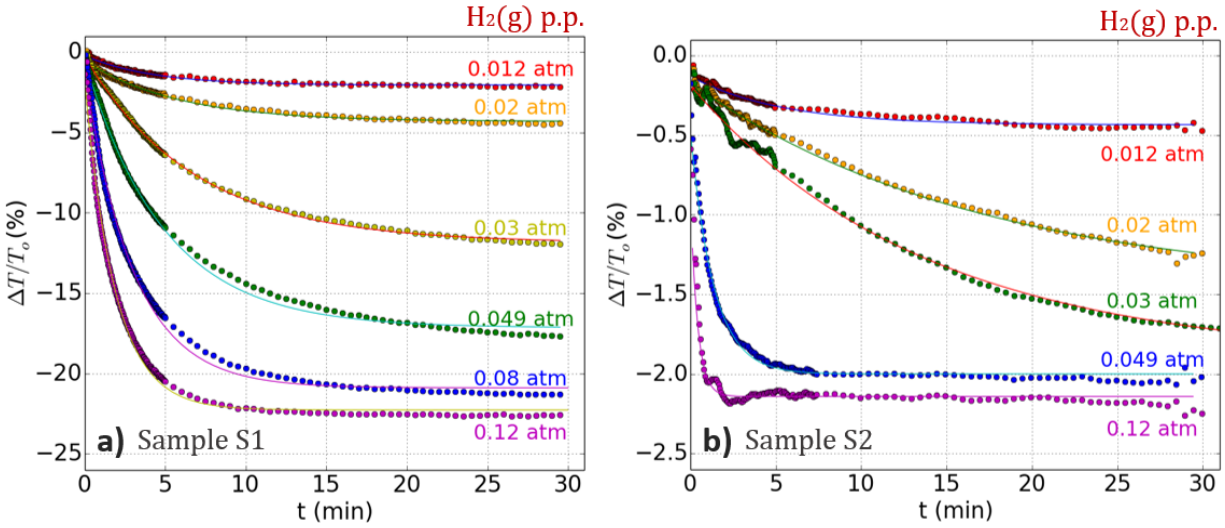

Figure 3.8: Relative variations in transmission ($\Delta T/T_0$; sensitivity) of sample S1 (a) and S2 (b) at several H_2(g) partial pressures exposures. The solid lines correspond to the fitting curves using eq. 3.1.

From Fig. 3.9 a) we clearly see that the obtained results are consistent with the known Pd-hydride α-β phase transition. For both samples, the shape of the curve $\Delta T_{eq}/T_0$ vs H_2 p.p. follows the profile of the Pd:H atomic ratio displayed in the pressure-composition isotherms, as shown in chapter 1 [16]. For low H_2 p.p. a relatively small $\Delta T_{eq}/T_0$ is measured. At this stage the Pd-hydride system achieves the equilibrium in a α-phase state (H:Pd < 0.015). However, once the H_2 p.p. increases above the critical α-β transition pressure, the β-phase domains start to be formed, associated with the higher H content (H:Pd ≈0.58), leading to the sharper decay in $\Delta T_{eq}/T_0$. In the case of sample S1, this is observed for the H_2 p.p. window between 0.02-0.04 atm. For higher H_2 p.p. (0.08-0.12 atm), the $\Delta T_{eq}/T_0$ curve tends to saturate due to the almost fully β-phase domains formation inside the Pd nanostructures. Therefore, the measurement of the $\Delta T_{eq}/T_0$ correlates reasonably well with the H content within the Pd nanostructures, allowing us to study the effects of the Pd-hydride phase transition, namely the kinetics of the Pd H absorption/desorption.

If we take this α-β transition into account, the characteristic time that the Pd samples needs to achieve the equilibrium, τ_{eq}, does not simply decrease with the higher H_2 concentration. In fact, as displayed in Fig. 3.9 b), τ_{eq} follows a non-monotonic behavior, revealing a maximum around the critical pressure where the α-β phase transition takes place, in agreement with others works

reported in the literature [35,69]. This is reasonable if we consider that the rate of H absorption is limited by the rate of H adsorption [21]. To understand this behavior we need to take into account first, the fact that the rate of H adsorption depends on the H_2(g) p.p. (see eq. 3.2), and second, the change in the H storage capacity exhibited by the Pd during the α-β phase transition. As the Pd hydride β-phase domains start to form, the sudden increase in the associated H:Pd atomic ratio (from 0.015 to 0.58 in the Pd bulk case) requires a higher amount of H to be absorbed by the Pd samples in order to reach the equilibrium state ($\Delta T_{eq}/T_0$) leading to the sudden increase of the τ_{eq}. After this, the H storage capacity remains fixed because the Pd is almost in β phase. Due to the increase in the H adsorption rate because of the increase of H_2(g) p.p. and the previous fact, a quicker achievement of the Pd hydride equilibrium state is obtained leading to the diminish in τ_{eq}. Finally the saturation shown in figure 3.9 for high H_2(g) p.p. can be explained because of the saturation of the H adsorption rate.

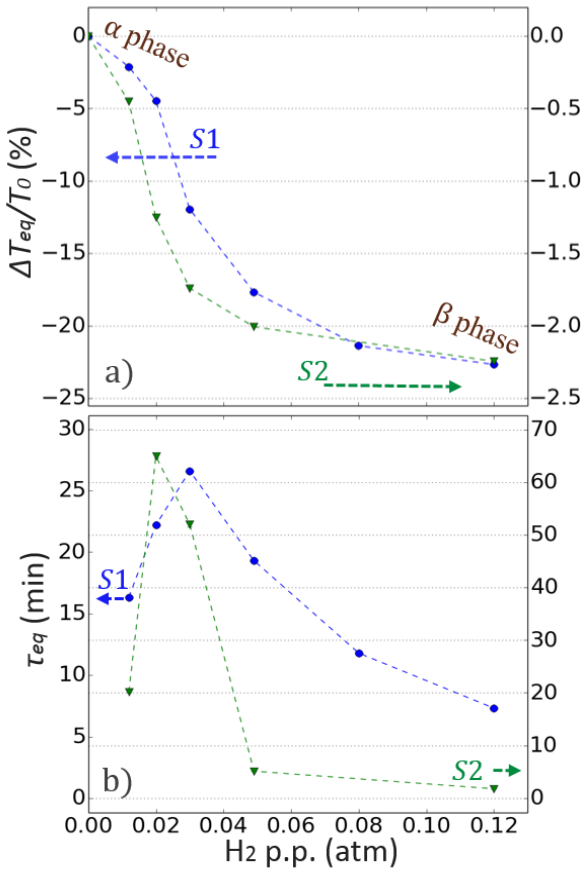

Figure 3.9: Sensors optical response as a function of the H_2(g) p.p. exposures and at a wavelength of 633 nm. a) Relative total variation in the transmitted light intensity measured once the system achieved the equilibrium state. b) The characteristic time response needed to achieve the equilibrium state, τ_{eq}.

If we look further into the obtained results, either from the data displayed in Figs. 3.9 a) or 3.9 b), we notice that the α-β phase transition associated with sample S2, solely composed with the

dendrites, has a sharper behavior and it occurs at lower pressures (0.01-0.03 atm) than for sample S1 (0.02-0.04 atm). From the SEM images, we know that sample S1 has a greater distribution in sizes than sample S2, with diameters ranging from 70 nm at NWs section down to 15-20 nm at the tips of the dendrites. This is in agreement with reported works in the literature, which have shown that the α-β phase transition hysteresis area and the critical α-β transition pressure both decrease with the Pd nanostructure´s size. [25,26]. For instance this phenomena, besides the higher surface to volume ratio, allows for sample S2 to achieve the equilibrium faster near the 4% explosive H_2(g) concentration threshold.

3.4.2 Study of the dehydrogenation of the Pd samples

In Fig. 3.10 it is shown the optical time response of the samples during the dehydrogenation cycles after the H_2(g) exposure (Fig. 3.8). It is observed for sample S1 (dendrites + NWs) that the β-α transition entails a high recovery time for the H desorption. This is not only due to the higher H content that has to be desorbed at the Pd surface[2], but also due to the fact that the β-α phase transition is an endothermic process [24] which means that energy is needed to destroy the formed β domains. Moreover, the formation of the β phase is associated with hysteresis, as illustrated at the inset of Fig. 3.10 a). The inset figure displays the optical response of the sample S1 ($\Delta T_{eq}/T_0$) to a stepped increase in the H_2 concentration exposure subsequently followed by a decrease.

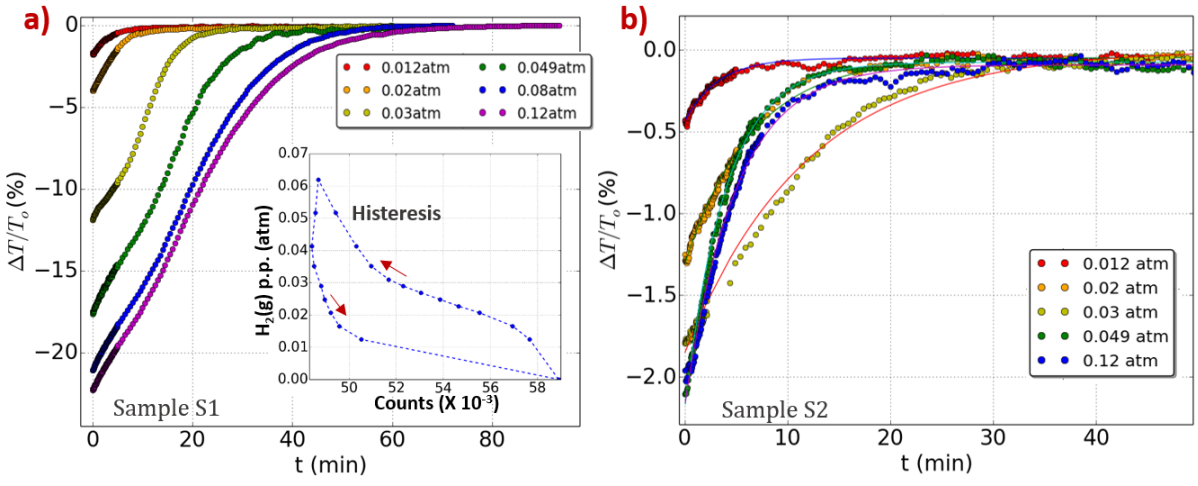

Figure 3.10: Relative variations in the transmission (ΔT/T0; sensitivity) of sample S1 (a) and S2 (b), during Pd dehydrogenation cycles performed for a pure N_2(g) atmosphere after several H_2(g) partial pressures exposures. The solid lines in b) correspond to fitting curves using eq. 3.1. The inset graph exhibits the optical response of the sample S1 to a stepped increase in the H_2 concentration exposure, subsequently followed by a decreasing in H_2 concentration.

[2] As the recombination of the H atoms chemically adsorbed at the Pd surface into the molecular H_2(g) correspond to an endothermic process [21,22].

In the case of the sample S1, we notice a delay in the H desorption only in the curves where the formation of the β phase domains (0.03-0.12 atm) takes place. Unlike the typical exponential behavior, as seen for the 0.012 atm curve, the H desorption curve at these pressures can be traced by two exponential desorption steps, as illustrated in Fig. 3.11 (eq. 3.1).

This desorption behavior is also observed in Ref. [35], where it is shown the change in resistivity of a nanostructured Pd thin film during the H desorption after the Pd hydride β-phase formation. Therefore, we are able to assume that this behavior is intrinsic to the thermodynamics of the dehydrogenation process and not originated for instance by a secondary optical effect. Either due to a sequential H desorption of the H atoms that remained with a high mobility in the α–phase state followed by a second desorption corresponding to the releasing of the H, which was originally trapped inside the stable β-domains, or even a sequential desorption dependent on the size and shape of the Pd nanostructures, namely of Pd dendrites followed by the NWs, both are suggested hypothesis that require a further investigation. In fact for sample S2, exclusively composed by the dendrites, this behavior is not observed. Additionally, it is seen that H desorption occurs faster for the pressures of 0.49 atm and 0.12 atm than for the previously measured 0.03 atm, as illustrated in Fig. 3.10 b). This possibly indicates a training effect present in the sample. The β phase formation and the related lattice constant expansion associated with an increase of 11% in the volume of the unit cell, may create new paths for H to diffuse, namely between grains of the Pd structure. This behavior is well known in the literature and Pd based sensors usually require an H_2(g) activation exposure in order to achieve repeatability . Comparing the 0.049 atm and 0.12 atm desorption curves of

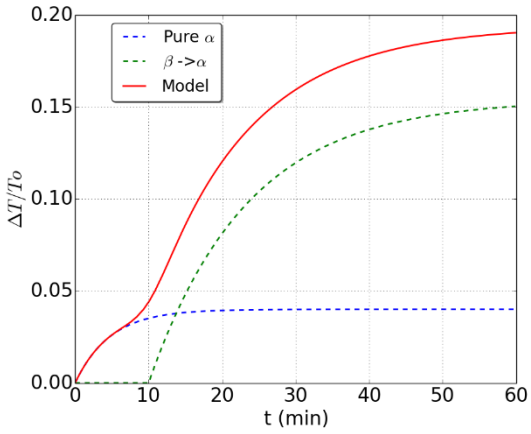

Figure 3.11: Illustration of a two-step sequential H desorption behavior. The Modelling curve correspond the sum of an exponential shaped hydrogen desorption, which is followed, after a 10 min delay, by a second H desorption (eq.3.1).

sample S2 with those of sample S1, a faster recovery of 20-30 min is observed for sample S2, contrasting with the 60-70 min of sample S1. This diminish is expected due to the higher surface to volume ratio of the Pd pure dendritic nanostructures.

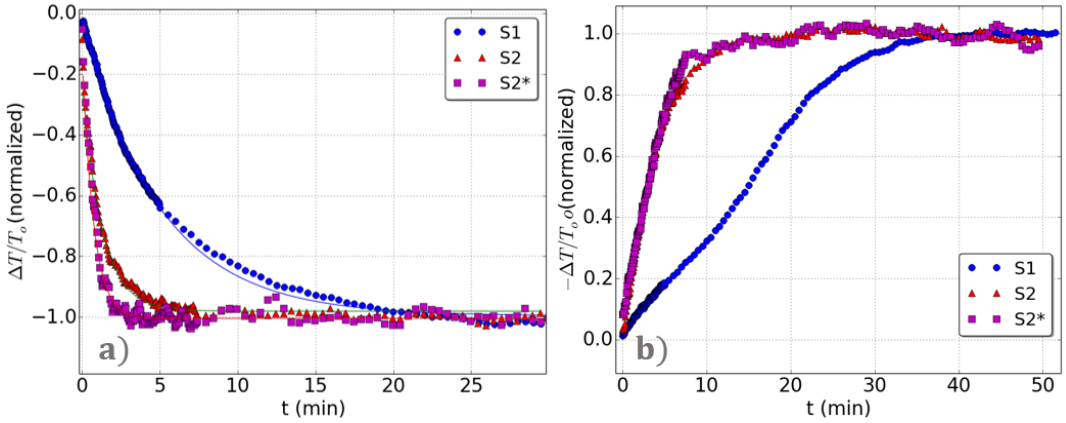

Figure 3.12: Comparison between the optical response of samples S1, S2 and S2* at a H_2 p.p. of 0.049 atm during a) H-absorption and b) H-desorption.

To analyze how the Pd dendrites exposed area affects to the hydrogenation/dehydrogenation behavior, it was performed in a twin S2 sample (S2*) a longer etching time of the alumina barrier (30 min). For a H_2 p.p. of 0.049 atm, we realize in Fig. 3.12 a) that by increasing the Pd exposed surface, we were able to reduce the time to achieve the equilibrium state (τ_{eq}) from 5 min to 2.5 min. On the other hand, if we look to the hydrogen desorption kinetics [Fig. 3.12 b)], any significant changes are not seen between samples S2 and S2*. This corroborates with the endothermic β-α phase transition being the time limiting process of the H-desorption. The discrepancy between the H desorption curves of samples S1 and S2(S2*) can be related to the formation of larger Pd hydride β-domains within the Pd structure of sample S1.

3.5 H_2(g) sensing operation modes

3.5.1 Stationary regime

Based on the previous behavior, we can define two different modes for hydrogen sensing, using Pd dendritic nanostructures. The most obvious one relies on measuring the total variation in transmitted light intensity once the Pd-hydride system achieves its equilibrium state, $\Delta T_{eq}/T_0$, (stationary regime). Due to the hysteresis observed in the transmission signal between H loading and unloading cycles [inset of Fig. 3.10 a); sample S1], the sensor should be implemented in an on-off sensing state in order to reduce the measurement uncertainty. In the on-state the sensor is exposed to a H_2(g) atmosphere until the respective transmitted light intensity stabilizes. For the off-state the sample is removed from the H_2(g) environment to allow the H desorption. As the kinetics of the H desorption are limited by the endothermic process of β-α transition and

the recombination of the H atoms at the Pd surface, this requires a recovery period of the order of tens of minutes. This recovery time can be diminished, for example by heating the Pd samples. For instance in 2014 the author Mazhar E. Nasirin reported a novel optical H sensor based on Core-shell Au-Pd NWs with recovering times of 45-30 s instead of 2 h, simply by heating their sensor with a 785 nm wavelength laser (100 mW/cm^2) [43]. Nevertheless, we were able to monitor hydrogen within the concentration range of 1-12%, achieving relative variations in transmitted intensities of the order of 23 % for sample S1 (10 times larger than sample S2) due to the higher content of Pd. On the other hand, comparing the kinetics of the H absorption/desorption, namely for H p.p. above the critical α–β transition pressure, sample S2 achieves its equilibrium Pd hydride state faster than sample S1 due to the higher surface to volume ratio, as well as it requires a shorter recovery time.

3.5.2 Transient regime

On a similar approach, we can also monitor H_2(g) by measuring the rate of transmission decay of the samples during the Pd-hydrogen absorption (transient regime). As it is known from the literature [21,22], the dissociation of the H_2 molecule and the chemical adsorption of H to the Pd surface corresponds to the limiting rate step for the H absorption. According to eq. 3.2, the rate of the H adsorption (r) will be higher for larger H_2 partial pressures:

$$r \propto exp\left(-{}^{E_a}/_{RT}\right) p_{H2}(\theta_*)^2, \tag{3.2}$$

where E_a corresponds to an energy barrier between the H-Pd physically and chemically adsorbed states, RT is the average kinetic energy, p_{H2} the H_2(g) partial pressure and θ_* the number of free-H surface sites at the Pd surface. In this way by choosing a specific cross-line value for the relative decay in the transmitted signal ($\Delta T/T_0$), we can measure how long it takes to achieve this state as a function of the H_2(g) partial pressure. It was chosen for sample S1 (S2) a relative decay in transmitted light intensity of 2% (0.4%), which corresponds to an almost pure α-phase for the Pd hydride structure, as previously shown in Fig. 3.9 a). The respective response times, $\tau_{2\%}$ and $\tau_{0.4\%}$, are plotted in Fig. 3.13.

It is observed that $\tau_{2\%}$ and $\tau_{0.4\%}$ curves follow a monotonic behavior, decreasing with the H_2 partial pressure. Therefore, in this transient regime we are able to detect in approximately 50 s the H_2 explosive threshold concentration of 4% of (v/v) in atmosphere. For higher H_2 p.p. the $\tau_{2\%}$ ($\tau_{0.4\%}$) tends to saturate. The reason for this behavior is related with an increase in the H-Pd surface coverage ratio, diminishing the available H-free Pd surface sites, for which the energy

barrier E_a between the H-Pd physically and chemically adsorbed states is minimum[3]. This limits the rate of the H adsorption as described in eq. 3.2 [21].

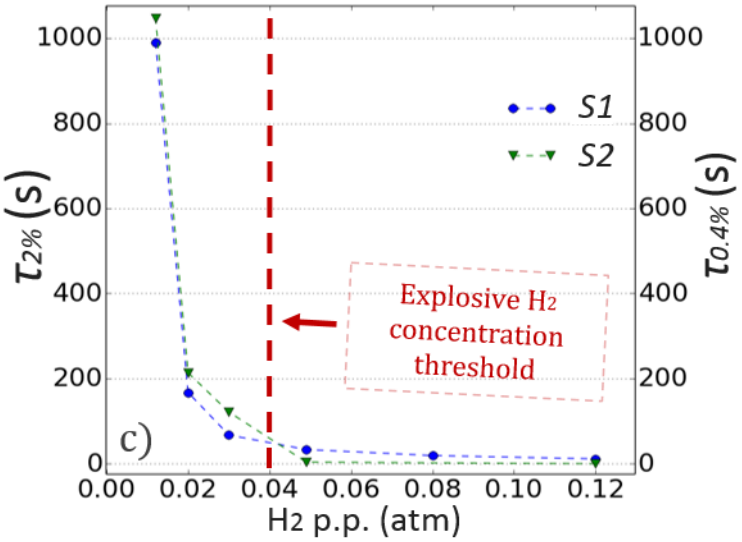

Figure 3.13 The response time of the samples S1 and S2 to achieve a transmission signal decay of 2% ($\tau_{2\%}$) and 0.4% ($\tau_{0.4\%}$), respectively.

Using again the on-off sensing scheme and by choosing a cross line corresponding to an almost pure α-state, we are able to reduce the response time of H_2(g) detection from minutes to tens of seconds within the range of 4-12% concentration. Additionally, if the measurement is interrupted before the beginning of the β-phase domains formation, as pretended here, this allow to reduce the recovery time from 70 min to 10 min in the case of sample S1. Moreover, when working with pure Pd based sensors, interrupting the β phase formation also has the advantage to increase the sensor's life-time as it enables to reduce hydrogen embrittlement effects [15].

[3] The H_2 molecules that impinge on Pd atoms that are already chemically bound to H atoms, encounter a higher energy barrier for the molecule dissociation [21].

Chapter 4

Conclusions and future work

The main objectives set for this thesis were accomplished, namely the fabrication of Pd nanostructures and their functionalization for H_2(g) sensing. A deeper understanding on the interaction of the H_2(g) and the Pd structures was gained throughout the experimental work.

The pulsed electrodeposition, assisted by anodic alumina templates, has shown to be a suitable method for the growth of Pd nanostructures. However, from the gathered results we have inferred that an undesired hydrogen-Pd co-deposition and its associated hydrogen embrittlement issues, have raised constrains in the time period of the PED process, limiting therefore the (maximum) average length of the grown Pd NWs. Also, it was shown that working with high deposition currents entails a higher inefficiency for the deposition (and a higher hydrogen co-deposition). At the same time it had the benefit of counterbalancing the inhomogeneity's in the AAO pore's electrical resistance, providing a more homogenous growth of the Pd nanostructures at the microscale. For the optimal tested conditions, we were able to obtain a 2.4 μm average NWs length associated with a relative length dispersion of 5.8%. In order to obtain a uniform distribution of NWs at longer dimensions further studies are required, namely those based on the impact of increasing the rest pulse time duration or the Pd ionic concentration.

During the Pd deposition a Fabry-Pérot light interference phenomena allowed us to monitor in real time the uniformity of the deposition process. Through the observation of the sample's progressive color changes, it was possible to infer the length of the Pd structure´s with the naked eye, within the range of 50 nm to 400 nm. This is especially useful for quality control, namely to ensure the fabrication of Pd based sensors with an uniform sensing response to H_2(g) across its region.

The thinning of the alumina barrier of the AAO templates, through the controlled non-steady state anodization process not only allowed us to electrodeposit metal NWs into Al foils through PED, but also it offered a simple method to functionalize the grown Pd nanostructures and AAO

template for H_2(g) optical sensing. The used technique relies purely on a self-assembly process that can be easily implemented at industrial level.

The characterization of the optical sensors was performed in transmission mode and its optical response was characterized according to the Pd hydride α–β phase transition. Two sensing modes were identified, using the transient and the stationary regimes of the Pd-hydrogenation cycles. In the α-phase transient regime, the sensor response time is of the order of tens of seconds within the H_2(g) concentration range of 4-12% (v/v) in atmosphere. The H_2(g) explosive threshold mixture of 4% (v/v) in atmosphere can be detected in 50 s, making this kind of optical sensor more suitable to work in conditions where the risk of explosion is eminent. On the other hand, in the stationary regime we were able to monitor H_2(g) concentrations within the range of 1-12% (v/v) in atmosphere. A maximum relative optical response of 23% is achieved at a wavelength of 633 nm for a 12% (v/v) H_2(g) concentration in atmosphere. For sensors working in this regime, it was also demonstrated the possibility of a faster detection (2.5 min) near the H_2 explosive threshold, using only dendritic nanostructures.

The limitation of the fabricated Pd sensors, rely primarily on the kinetics of the Pd hydrogen absorption/desorption. The AAO template although offers a simple method to functionalize the Pd nanostructures, at the same time it reduces the effective Pd exposed surface, limiting the rate of the H adsorption. To overcome this issue it is suggested as a future work the electrodeposition of Pd NWs through the direct current method (DC). Furthermore, the deposition of Pd NWs into cathodic Au/Ti films will enable the dissolution of the AAO template and the achievement of fully exposed free standing Pd NWs. Also the H desorption times of the order of tens of minutes can be diminished by the electrodeposition of Pd alloys, such as PdNi or PdAu NWs, improving the performance of these type of sensors. In fact the chemical destabilization of the β phase formation, besides increasing the rate of the H desorption, has also the ability of increasing the H_2(g) concentration measurement range up to 0-100% (v/v) in atmosphere, as well to reduce the measurement uncertainty associated with the β–phase formation.

References

[1] A Züttel, A Remhof, A Borgschulte and O Friedrichs, Hydrogen: the future energy carrier, *Phil. Trans. R. Soc. A* **368**, 3329–3342 (2010)

[2] Ram B Gupta *Hydrogen Fuel: Production, Transport, and Storage*, CRC Press, 0th Edition, 2008; chap. 15

[3] http://www.nasa.gov/topics/technology/hydrogen/index.html (accessed 1/5/2015)

[4] Andrew Bocarsly and David Michael P Mingos (Editors) *Fuel Cells and Hydrogen Storage (Structure and Bonding)*, Springer, 2011

[5] G W Crabtree, M S Dresselhaus and M V Buchanan, The hydrogen economy, *Physics Today* **57**(12), 39 (2004)

[6] A Züttel, A Borgschulte and L Schlapbach, *Hydrogen as a Future Energy Carrier*, Wiley-VCH; 1st edition, 2008

[7] H Robatjazi, S M Bahauddin, C Doiron, and I. Thomann, Direct Plasmon-Driven Photoelectrocatalysis *Nano Lett.*, **15** (9), 6155–6161 (2015)

[8] M M May, H J Lewerenz, D Lackner, F Dimroth and T Hannappel, Efficient direct solar-to-hydrogen conversion by in situ interface transformation of a tandem structure. *Nat. Commun*. **6**, 8286 (2015)

[9] http://www.h-tec.com/en/education/technology/fuel-cells/ (accessed 1/5/2015)

[10] https://h2tools.org/bestpractices/h2properties (accessed 1/5/2015)

[11] http://www1.eere.energy.gov/hydrogenandfuelcells/mypp/pdfs/safety.pdf (accessed 1/6/2015)

[12] W J Buttner, M B Post, R Burgess and C Rivkin, An overview of hydrogen safety sensors and requirements, *Int. J. Hydrogen Energ.*, **36** 2462 -2470 (2011)

[13] G Alefeld and J Völkl (Editors), *Hydrogen in Metals I: Basic Properties Topics in Applied Physics (Book 28)*, Springer, Edition 2013

[14] G Alefeld and J Völkl (Editors), *Hydrogen in Metals II: Application-Oriented Properties Topics in Applied Physics (Book 29)*, Springer, Edition 2013

[15] H C Rogers, Hydrogen embrittlement of metals: atomic hydrogen from a variety of sources reduces the ductility of many metals, *Science* **159** 1057–1064 (1968)

[16] F A Lewis, *The Palladium Hydrogen System*, Academic Press, New York, 1967

[17] F A Lewis, The Hydrides of Palladium and Palladium Alloys, *Platinum Metals Rev.*, **4**(4), 132 (1960)

[18] S Yuna, S T Oyama, Correlations in palladium membranes for hydrogen separation: A review, *J. Membrane Sci.* **375**, 28–45 (2011)

[19] V Berube, Size effects on the hydrogen storage properties of nanostructured metal hydrides: a review *Int. J. Energy Res.* **31**, 637–663 (2007)

[20] http://hydropole.ch/en/hydrogen/storage/ (accessed 2/3/2015)

[21] N Lopez, Z Łodziana, F Illas and M Salmeron, When Langmuir Is Too Simple: H2 Dissociation on Pd(111) at High Coverage, *Phys. Rev. Lett.*, **93**, 146103 (2004)

[22] M Lischka and A Groß, Hydrogen on palladium: A model system for the interaction of atoms and molecules with metal surfaces, *Recent Developments in Vacuum Science and Technology*, Research Signpost, 2003, chap. 7

[23] I-yuan Wei and J Brewer, Desorption of Hydrogen from Palladium Plating, *AMP Journal of Technology* **5**, 49-53 (1996)

[24] R Gremaud, M Slaman, H Schreuders, B Dam and R Griessen, An optical method to determine the thermodynamics of hydrogen absorption and desorption in metals. *Appl. Phys. Lett.* **91**, 231916 (2007)

[25] A Baldi, T C Narayan, A L Koh and J A Dionne, In situ detection of hydrogen-induced phase transitions in individual palladium nanocrystals, *Nat. Mater.* **13**, 1143–1148 (2014)

[26] R Bardhan, L O Hedges, C L Pint, A Javey, S Whitelam and J J Urban, Uncovering the intrinsic size dependence of hydriding phase transformations in nanocrystals *Nat. Mater.* **12**, 905–912 (2013)

[27] T Mütschele, R Kirchheim, Segregation and diffusion of hydrogen in grain boundaries of palladium, *Scripta Metall. Mater.*, **21**(2), 135-140 (1987)

[28] U Stuhr, H Wipf, T J Udovic, J Weissmu¨ller and H Gleiter, *J. Phys. Cond. Matter* **7**, 219 (1995)

[29] C Sachs, A Pundt, R Kirchheim, M Winter, M T Reetz and D Fritsch, Solubility of Hydrogen in Single-Sized Palladium Clusters. *Phys. Rev. B* **64**, 075408 (2001)

[30] A Houari, S F Matar, and V Eyert, Electronic structure and crystal phase stability of palladium hydrides, *J. Appl. Phys.* **116**, 173706 (2014)

[31] W E Vargas, I Rojas, D E Azofeifa, and N Clark, Optical and electrical properties of hydrided palladium thin films studied by an inversion approach from transmittance measurements. *Thin Solid Films* **496**, 189-196 (1996)

[32] J Isidorsson, I A M E Giebels, H Arwin and R Griessen, Optical properties of MgH2 measured in situ by ellipsometry and spectrophotometry. *Phys. Rev. B* **68**, 115112 (2003)

[33] P Offermans, H D Tong, C J M van Rijn, P Merken, S H Brongersma and M Crego-Calama, Ultralow-power hydrogen sensing with single palladium nanowires, *Appl. Phys. Lett.* **94**, 223110 (2009)

[34] X Q Zeng, M L Latimer, Z L Xiao, S Panuganti, U Welp, W K Kwok and T Xu, Hydrogen Gas Sensing with Networks of Ultrasmall Palladium Nanowires Formed on Filtration Membranes. *Nano Lett.***11**, 262-268 (2011)

[35] X Q Zeng, Y L Wang, H Deng, M L Latimer, Z L Xiao, J Pearson, T Xu, H H Wang, U Welp, G W Crabtree and W K Kwok, Networks of Ultrasmall Pd/Cr Nanowires as High Performance Hydrogen Sensors. *ACS Nano* **5**, 7443-7452 (2011)

[36] K T Kim, S J Sim and S M Cho, Hydrogen Gas Sensor Using Pd Nanowires Electro-Deposited Into Anodized Alumina Template, *IEEE Sens. J.* **6**(3), 509-513 (2006)

[37] I Pavlovsky, Hydrogen Sensor for Oil Transformer Health Monitoring, *8th IEEE Conference on Nanotechnology*, 211 – 213 (2008)

[38] M Ameen Poyli, V M Silkin, I P Chernov, P M Echenique, R Díez Muiño and J Aizpurua, Multiscale Theoretical Modeling of Plasmonic Sensing of Hydrogen Uptake in Palladium Nanodisks, *J. Phys. Chem. Lett.***3**, 2556−256 (2012)

[39] R R J Maier, B J S Jones, J S Barton, S McCulloch, T Allsop, J D C Jones and I Bennion, Fibre optics in palladium-based hydrogen sensing. *J. Opt. A: Pure Appl. Opt.* **9**, S45-S59 (2007)

[40] M A Butler, Optical fiber hydrogen sensor, *Appl. Phys. Lett.* **45**, 1007-1009 (1984)

[41] C Perrotton, R J Westerwaal, N Javahiraly, M Slaman, H Schreuders, B Dam and P Meyrueis, A reliable, sensitive and fast optical fiber hydrogen sensor based on surface Plasmon resonance. *Opt. Express* **21**, 382-390 (2013)

[42] A Tittl, P Mai, R Taubert, D Dregely, N Lui and H Giessen, Palladium-Based Plasmonic Perfect Absorver in the Visible Wavelength Range and its Application to Hydrogen Sensing, *Nano Lett.***11**, 4366-4369 (2011)

[43] M E Nasir, W Dickson, G A Wurtz, W P Wardley and A V Zayats, Hydrogen detected by the naked eye: optical hydrogen gas sensors based on core/shell plasmonic nanorod metamaterials. *Adv. Mater.***26**, 3532-3537 (2014)

[44] C Wadell, F A A Nugroho, E Lidstro, B Iandolo, J B Wagner and C Langhammer, Hysteresis-Free Nanoplasmonic Pd−Au Alloy Hydrogen Sensors, *Nano Lett.* **15**, 3563−3570 (2015)

[45] K Nielsch, F Müller, An-Ping Li and U Gösele, Uniform Nickel Deposition into Ordered Alumina Pores by Pulsed Electrodeposition, *Adv. Mater.* **12** (8), 582-586 (2000)

[46] H Masuda and K Fukuda, Ordered Metal Nanohole Arrays Made by a Two-Step Replication of Honeycomb Structures of Anodic Alumina. *Science* **268**, 1466-1468 (1991)

[47] M Aliofkhazraei (Editor), *Modern Surface Engineering Treatments*, InTech, 2013

[48] D Losic and A Santos, *Nanoporous Alumina: Fabrication, Structure, Properties and Applications*, Springer, 2015

[49] C T Sousa, *Development of Nanoporous Alumina Templates for Biotechnological Applications*, Ph.D. Thesis, Department of Physics and Astronomy, Faculty of Sciences of the University of Porto, 2011

[50] O Jessensky, F Müller and U Gösele, Self-organized formation of hexagonal pore arrays in anodic alumina, *Appl. Phys. Lett.* 72, 1173 (1998)

[51] L Assaud, S Bochmann, S Christiansen and J Bachmann, A large electrochemical setup for the anodization of aluminum towards highly ordered arrays of cylindrical nanopore, *Rev. Sci. Instrum.* 86, 073902 (2015)

[52] G Sauer, G Brehm, S Schneider, K Nielsch, R B Wehrspohn, J Choi, H Hofmeister and U Gösele, Highly ordered monocrystalline silver nanowire arrays. *J. Appl. Phys.* **91**, 3243 (2002)

[53] R C Furneaux, W R Rigby and A P Davidson, The formation of controlled porosity membranes from anodically oxidized aluminum, *Nature* **337**, 147 – 150 (1989)

[54] C T Sousa, D C Leitão, M P Proença, A Apolinário, J G Correia, J Ventura and J P Araújo, Tunning pore filling of anodic alumina templates by accurate control of the bottom barrier layer thickness, *Nanotech*. **22**, 315602 (2011)

[55] C T Sousa, A Apolinário, A M Pereira, J Ventura and J P Araújo, Precise control of the filling stages in branched nanopores, *J. Mater. Chem.* **22**, 3110-3116 (2012)

[56] J Azevedo, C T Sousa, A Mendes and J P Araújo, Influence of the Rest Pulse Duration in Pulsed Electrodeposition of Fe Nanowires, *J. Phys. Chem. C* **115**, 8567–72 (2011)

[57] J Azevedo, C T Sousa, J Ventura, A Apolinario, A Mendes and J P Araujo, Ultra-long Fe nanowires by pulsed electrodeposition with full filling of alumina templates, *Mater. Res. Express* **1**, 015028 (2014)

[58] D C Leitao, C T Sousa, J Ventura, J S Amaral, F Carpinteiro, K R Pirota, M Vazquez, J B Sousa and J P Araujo, Characterization of electrodeposited Ni and Ni80Fe20 nanowires, *J. Non-Cryst. Sol.* **354**, 5241 (2008)

[59] D C Leitao, A Apolinario, C T Sousa, J Ventura, J B Sousa, M Vazquez and J P Araujo, Nanoscale Topography, A Tool to Enhance Pore Order and Pore Size Distribution in Anodic Aluminum Oxide, *J. Phys. Chem. C* **115**(17), 8567–8572 (2011)

[60] N Tasaltın, S Ozturk, N Kılınc¸H Yuzer and Z Z Ozturk, Fabrication of vertically aligned Pd nanowire array in AAO, *Nanoscale Res Lett* 5, 1137–1143 (2010)

[61] V Vega, J Garcia, W O Rosa, L G Vivas, V M Prida, B Hernando and M Vázquez, Magnetic Properties of (Fe, Co)–Pd Nanowire Arrays, *J. Nanosci. Nanotechno.* **12**(9), 7501-4 (2012)

[62] M Schlesinger and M Paunovic, *Modern Electroplating 5th Edition*, Wiley; Fifth Edition, John Wiley & Sons, Inc., Hoboken, NJ, USA, 2014

[63] K J Bryden and J Y Ying, Pulsed Electrodeposition Synthesis and Hydrogen Absorption Properties of Nanostructured Palladium-Iron Alloy Films, *J. Electrochem. Soc.* **145**, 10 (1998)

[64] A Marashdeh, First–Principles Study Including Zero Point Energy on Hydrogen in Palladium for Hydrogen Membranes Applications, *Advanced Materials Research* **875-877**, 635-641 (2014)

[65] E Hecht, *Optics 4th Edition*, Addison-Wesley, 2001

[66] W Cai and V Shalaev, *Optical Metamaterials: Fundamentals and Applications*, 2010 edition Springer, 2009

[67] https://people.ifm.liu.se/boser/elma/ (accessed 5/11/2014)

[68] A Hierro-Rodriguez, I T Leite, P Rocha-Rodrigues, P Fernandes, J P Araujo, J L Santos, J M Teixeira and A Guerreiro, Hydrogen sensing via anomalous optical absorption of Pd-based metamaterial, submitted to Nanotechnology

[69] F Yang, S C Kung, M Cheng, J C Hemminger and R M Penner, Smaller Is Faster and More Sensitive: The Effect of Wire Size on the Detection of Hydrogen by Single Palladium Nanowires. *ACS Nano*, **4**, 5233–5244 (2010)

Appendix A

The AAO template correspond to a composite material, it is an organized structure consisting in a mixture of Alumina and air (or electrolyte). In this case the alumina material corresponds to the host matrix while the air or the grown NW´s within the AAO template are named as the inclusions. When dealing with composite materials if the dimensions of the inclusions and of the gaps between them are significantly lower than the wavelength of the visible light, the collective response of the composite can be approximated as the response of an homogenous medium, characterized by an effective refractive index [66]. We are allowed to use these homogenizations approaches, such as the homogenization Maxwell Garnett model, as the characteristic AAO template structural parameters, namely the AAO lattice parameter (a) and pore diameter (d_p), are typically smaller than the optical wavelengths ($a \approx 100$ nm and $d_p \approx 35$ nm).

$$\varepsilon_{eff} = \varepsilon_h \frac{1+\eta\Gamma}{1-\Gamma} \quad , \quad \Gamma = \sum_{i=1}^{N} f_i \frac{\varepsilon_i - \varepsilon_h}{\varepsilon_i + \eta\varepsilon_h}, \tag{A.1}$$

Equations A.1 correspond to the effective electric permittivity (ε_{eff}) expressions of the Maxwell Garnett model, respectively for an arbitrary number N of material inclusions. Where f_i and ε_i represent respectively the fill ratio and electric permittivity of the i-th inclusion (Pd or air), ε_h is the electric permittivity of the host medium (AAO template) and η is the screening factor of the inclusions. This last one depends on the inclusion's shape regarding to electric field orientation and is defined as $\eta = L^{-1} - 1$, where L is the Lorentz depolarization factor.

A.1 Fabry-Pérot considerations

During the course of the electrodeposition the complete AAO template can be regarded as a two separate homogenous mediums, the Pd filled-AAO and the electrolyte filled-AAO template. The Maxwell–Garnett homogenization model predict that the effective refractive index (ε_{eff}) of a composite such as the AAO template will change if either filled with Pd ($\tilde{n}_{AAOPd}$) or filled with electrolyte/air ($\tilde{n}_{AAOAir}$). Thus from the Fresnel´s law of reflection, the resulting refractive index difference provides the reflectivity (R_2) associated with the AAO-Pd/AAO-Electrolyte interface [65]. As for the reflectivity of mirror M1 is provided by refractive index difference between the Al substrate and AAO-Pd template.

$$R_1 = \left(\frac{\tilde{n}_{AAOPd} - \tilde{n}_{Al}}{\tilde{n}_{AAOPd} + \tilde{n}_{Al}}\right)^2 \quad ; \quad R_2 = \left(\frac{\tilde{n}_{AAOPd} - \tilde{n}_{AAOAir}}{\tilde{n}_{AAOPd} + \tilde{n}_{AAOAir}}\right)^2 \qquad \text{(A.2)}$$

It was developed a Python program based on the transfer matrix method to perform the correspondent calculation of the Reflectance spectra [67]. At first, through the A.1 equations, the algorithm returns the ε_{eff} both for the AAO-Pd and the AAO-Air template. It was assumed a the screening factor = 1, and a fill ratio for the inclusions (f_i) equal to the measured porosity of the AAO templates (≈ 0.11).

Subsequently according to the obtained $\tilde{n}_{AAOPd}$ and $\tilde{n}_{AAOair}$ an algorithm based on the transfer matrix method [67] calculates the Reflectance Spectra for the equivalent multilayer model as depicted in the configuration presented in Fig. A.1.

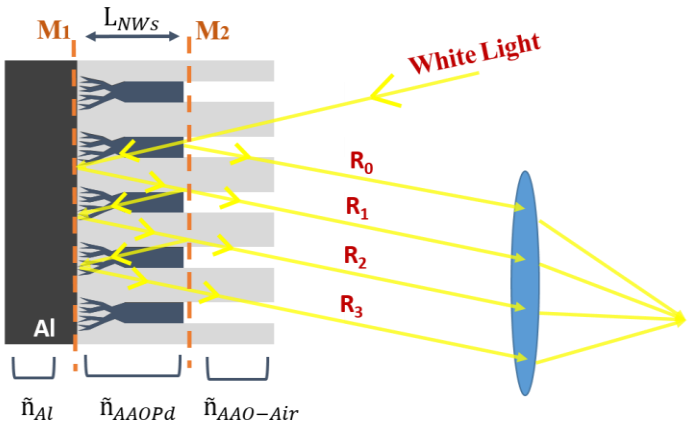

Figure A.1 Configuration of the Multilayer Model for the calculation of the Reflectance spectra.